

1

2

3 This manuscript is a **preprint** and has been submitted to be considered for publication in
4 **Basin Research**. This version of the manuscript has not undergone peer review. Content in
5 subsequent versions of this manuscript may differ from this version of the work.

6 Please contact James Wood (james.wood18@imperial.ac.uk) or any of the study co-authors
7 directly for questions relating to the manuscript.

8

9

Fault migration and basin evolution during complex rifting: examples from the western North Gulf of Evia, Greece

James Wood¹, Rebecca E. Bell¹, Alexander C. Whittaker¹, Saoirse M. Coveney¹, Frank Chanier², Fabien Caroir³, Haralambos D. Kranis⁴, Athanassios Ganas⁵

¹ Department of Earth Science & Engineering, Imperial College London, London, UK

² Laboratoire d'Océanologie et de Géosciences, Univ. Lille, CNRS, Univ. Littoral Côte d'Opale, Lille, France

³ Institut des Sciences de la Terre de Paris, Sorbonne Université, CNRS-INSU, Paris, France

⁴ Department of Dynamic, Tectonic & Applied Geology, National and Kapodistrian University of Athens, Athens, Greece

⁵ Institute of Geodynamics, National Observatory of Athens, Athens, Greece

Corresponding author: James Wood (james.wood18@imperial.ac.uk)

Acknowledgements

This work received funding as part of the TALENTS doctoral network through the European Union's HORIZON-MSCA-2022-DN-01 research and innovation program under grant agreement No. 101119486 (<https://www.talents-dn.eu>). JW, AW, RB, HK, and AG are beneficiaries of this grant. SC is funded by NERC grant NE/S007415/1 (Science and Solutions for a Changing Planet DTN). We are grateful to SLB for the provision of Petrel (Version 2024.4.0) for use in this project.

31 Abstract

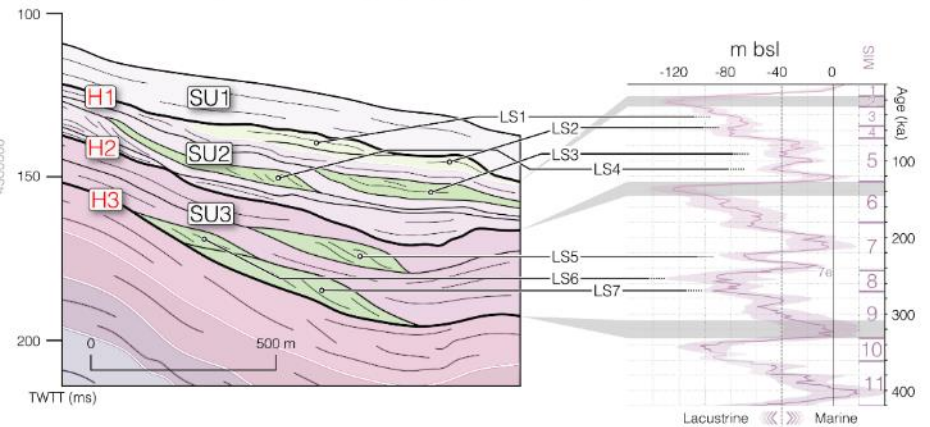
32 Understanding dynamic processes of faulting and basin evolution across timescales in
33 complex rift settings remains a key challenge in active continental tectonics. This is in part
34 due to a limited number of young rift systems with well constrained, high-resolution age
35 models derived from subsurface datasets. We aim to address this challenge and advance our
36 understanding of time-dependent geodynamic rift processes by developing a late-Quaternary,
37 syn-kinematic age model for the Western Basin of the North Gulf of Evia, Central Greece. In
38 contrast to the nearby Gulf of Corinth, extension here is complicated by rotational and strike-
39 slip influence from the westward-propagating North Anatolian Fault. Seismic stratigraphic
40 principles are used to identify three key horizons based on reflection termination relationships
41 with ages of ~12 ka, ~130 ka and ~325 ka assigned through a sequence stratigraphic model
42 on deltaic clinoform packages. The age model is applied alongside a network of offshore
43 faults to determine the major structures, depocenters and evolutionary history of the rift. We
44 resolve the major controlling faults to be the Kalypso Fault (~4 mm/yr slip) at the southern
45 margin of the basin and the Central Graben (~1-2 mm/yr slip) along the axis of the gulf. We
46 show that the Kalypso Fault is linked to the onshore Coastal Fault System following a
47 migration event with evolving strike from the onshore Arkitsa Fault. The timing of this event
48 is constrained to ~325 ka based on hanging wall sediment thickening relationships and the
49 Kalypso Fault displays immediate, rapid lateral growth and throw accumulation after
50 initiation. Improved constraints on the timing and evolutionary behaviour of young normal
51 fault systems such as this show that fault migration and activation in complex rift settings can
52 occur over timescales less than 10^5 years.

53 Graphical Abstract

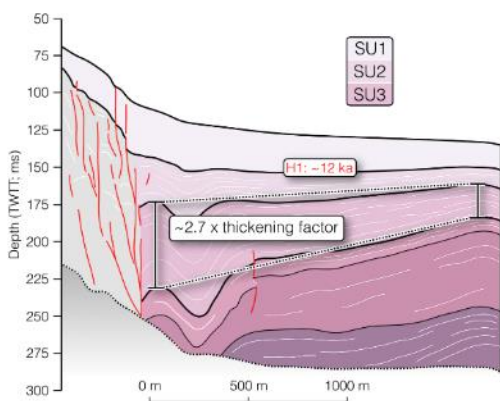
The North Gulf of Evia rift:
Tectonic overview map



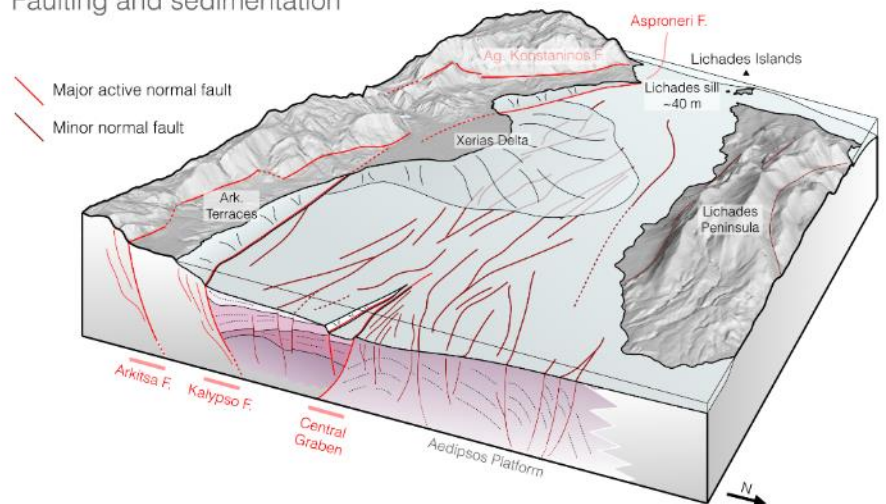
Methods - Age model:
Seismic and sequence stratigraphy (0 - 325 ka)



The Kalypso Fault:
Major offshore syn-kinematic
normal fault zone



Western Basin overview:
Faulting and sedimentation



54 1. Introduction

55 Understanding the timing of fault initiation and strain localisation in rifts is of key importance
56 for constraining models of continental extension, syn-tectonic basin evolution, and seismic
57 hazard. However, as young continental rifts are some of the most dynamic tectonic systems
58 on Earth (Brune et al., 2023), any detailed reconstruction of the timing of fault initiation,
59 linkage and migration typically demands a high-resolution age model of syn-kinematic
60 stratigraphy (Gawthorpe and Leeder, 2000). However, available age models in active rifts at

61 sufficient detail to allow fault slip rates and timings of initiation, linkage and migration to be
62 resolved over high-resolution timescales (10^3 - 10^4 years) are sparse.

63 Rifting is rarely a simple process, as fault systems may develop oblique to extensional strain
64 (e.g., Agostini et al., 2009; Brune, 2014; Jourdon et al., 2020), basement inheritance can
65 influence fault system growth and migration (e.g., Brune et al., 2017; Molnar et al., 2017;
66 Phillips et al., 2019), and crustal block rotation can introduce evolving principal stress
67 orientations in the rift (e.g., Bradley et al., 2013; Zwaan et al., 2020; Zwaan and Schreurs,
68 2020). Temporal and spatial reconstructions of normal fault dynamics from natural examples
69 in complex and rotational rift settings are extremely limited at present and high-resolution
70 age models are required to unlock detailed study into the geodynamics and mechanics of
71 these systems.

72 Syn-rift sedimentation in evolving basins, typically imaged at depth with seismic reflection
73 data, provides an integrated, but often complex, record of both tectonic and environmental
74 forcing (Gawthorpe and Leeder, 2000). However, where tectonic signals can be isolated
75 effectively, for instance through the reconstruction of prevailing environmental conditions
76 (e.g., base level), analysis of syn-rift stratigraphy can provide powerful, quantitative insights
77 into slip rates and evolution of normal fault systems (e.g., Bell et al., 2009, 2008; Feng et al.,
78 2016; Gawthorpe et al., 2018; Nixon et al., 2024, 2016).

79 The Gulf of Corinth, Greece represents one of the only marine continental rift systems with a
80 high-resolution age model thanks to extensive high-resolution seismic reflection datasets (see
81 Nixon et al., 2016) and deep offshore drilling (McNeill et al., 2019; Nixon et al., 2024). The
82 age models developed for the Gulf of Corinth generated a framework for the rift to become
83 one of the foremost natural laboratories for the detailed study of normal faulting processes
84 (e.g., Bell et al., 2017; de Gelder et al., 2019; Fernández-Blanco et al., 2019; Mildon et al.,

85 2024) and basin sedimentation (e.g., Gawthorpe et al., 2017; McNeill et al., 2019; Watkins et
86 al., 2018). However, the geodynamics of rifting in the Gulf of Corinth are relatively simple.
87 Extension is orthogonal to the rift system, the evolution of the rift is controlled by the basin-
88 ward migration of sub-parallel normal fault systems, and strike-slip associations are limited
89 (Ford et al., 2017; Gawthorpe et al., 2018; Leeder et al., 2008; Nixon et al., 2024, 2016).

90 The North Gulf of Evia, located ~100 km north of the Gulf of Corinth, provides an example
91 of a contrasting style of complex rifting to Corinth and represents a key extensional system in
92 Central Greece (Figure 1). Here, rifting is complicated by marked rotational and strike-slip
93 influence from the westward-propagating North Anatolian Fault (Caroir et al., 2024; Ganas et
94 al., 2016; Hatzfeld et al., 1999; Sboras et al., 2025) and the complexity of the system is
95 exaggerated by oblique fault systems (Kranis et al., 2001; Palyvos et al., 2006), asymmetric
96 normal fault geometries (Goldsworthy et al., 2002), and the reactivation of inherited Alpine
97 structures (Chanier et al., 2024; Kranis, 2007). The North Gulf of Evia therefore provides an
98 excellent opportunity to advance our understanding of rifting and normal faulting processes
99 when coupled with geodynamic or lithospheric complexity.

100 In this study we utilise a high-density, high-resolution 2D seismic reflection dataset to
101 develop a consistent seismic and sequence stratigraphic age model for late-Quaternary syn-
102 tectonic sedimentation (0 – ~325 ka) of the western North Gulf of Evia (Figure 2). A new
103 offshore network of normal faults is mapped, and we apply the age model to reconstruct a
104 detailed, late-Quaternary history of fault slip and basin development in the Western Basin of
105 the Gulf. Normal fault migration processes are examined in detail in relation to the
106 continental rotation in the Western Basin and in doing so, the work sheds new detailed insight
107 into the temporal evolution of complex rift systems over timescales of 10^4 - 10^5 years.

108 2. Geological Background

109 2.1 Tectonic setting

110 The North Gulf of Evia is one of a series of young, ~E-W striking rift systems spanning the
111 continental block of mainland Greece (Figure 1; Goldsworthy et al., 2002; Papanikolaou,
112 2021; Roberts and Ganas, 2000; Roberts and Jackson, 1991). Extension is thought to be
113 controlled by the rollback of a shallowly subducting African Plate (Jolivet et al., 2013) with
114 regional influence from the westward-propagation of the North Anatolian Fault and westward
115 extrusion of the Anatolian Plate (Figure 1; Caroir et al., 2024; Goldsworthy et al., 2002;
116 Hatzfeld et al., 1999; Sboras et al., 2025). This influence is responsible for 5-8°/Myr rotation
117 of the continental block between the gulfs of Evia and Corinth (Bradley et al., 2013; Briole et
118 al., 2021; Chousianitis et al., 2024) and the extensive strike-slip associations in the North
119 Gulf of Evia (Figure 2; Caroir et al., 2024; Ganas et al., 2016; Kranis et al., 2001; Palyvos et
120 al., 2006).

121 Although modern geodetic opening rates of 2.9-3.7 mm/yr (Sboras et al., 2025) are ~4 times
122 slower than in the neighbouring Corinth Rift (Briole et al., 2021; Chousianitis et al., 2024),
123 large, damaging earthquakes are known to have occurred around the North Gulf of Evia
124 including the 1894 Atalanti events (Mw 6.4-6.9; Ganas et al., 1998; Pantosti et al., 2004) and
125 the unattributed tsunami-generating earthquake of 426 BCE (Freitag and Reicherter, 2019).

126 The modern tectonic geometry of the North Gulf of Evia is divided into the Western, Central
127 and Eastern Basins based on bathymetric and subsurface character (Sakellariou et al., 2007;
128 Fig. 1b). Here we consider the Western Basin, a sub-basin at the margin of the gulf between
129 the Coastal Fault System and the Lichades Peninsula (Figure 2b) with the highest extensional
130 strain accommodation in the gulf (~3.7 mm/yr; Sboras et al., 2025). The Coastal Faults span

131 from Arkitsa to beyond Kammena (*or Kamena*) Vourla (~30 km) as a segmented but linked
132 onshore active normal fault array with a late-Quaternary footwall-component uplift rate of
133 0.2-0.6 mm/yr (Whittaker and Walker, 2015). The fault system is typically considered the
134 most active structure of the modern rift (Goldsworthy et al., 2002; Roberts and Jackson,
135 1991). The segments of the Coastal Faults vary in orientation and dip but ubiquitously
136 display north-oriented slip vectors (Figure 2b; Kranis 2007).

137 Despite evidence for Holocene slip on the Coastal Faults (Kranis, 2007), the geomorphology
138 of the hanging wall land strip shows evidence for rapid uplift (c.f. Wood et al., 2025). This
139 includes the uplifted marine terraces at Arkitsa (Figure 2b) and Holocene coastal notches at
140 Kynos (Supplementary Figure S1) which may indicate the dominant normal faults have
141 migrated offshore (Papanastassiou et al., 2014; Pirazzoli et al., 1999).

142 2.2 Pleistocene palaeoenvironment

143 Sedimentation in basins is a record of prevailing relative sea, lake or river level (Vail et al.,
144 1977). Isolating tectonic signals from the sedimentary packages imaged in seismic reflection
145 data demands a comprehensive reconstruction of environmental conditions (e.g., base level,
146 sill level and sedimentary environment).

147 The North Gulf of Evia is a semi-enclosed basin with distinct marine, lacustrine and brackish
148 intervals over the late-Quaternary controlled by sills in the Oreoi and Lichades Straits at 40-
149 45 m bsl (below mean sea level; Figure 2b). Intervals where eustatic sea level is below sill
150 level are interpreted as lacustrine or brackish in the Gulf and eustatic highstands above ~40 m
151 bsl are considered marine. It is probable that most of the Pleistocene lakes of the North Gulf
152 of Evia were restricted to the deepest part of the basin where many submerged terraces have
153 been mapped in vintage seismic datasets (Van Andel and Perissoratis, 2006).

154 The sill level at Lichades (Figure 2b) has likely varied over time. InSAR-derived ground
155 motion data indicates ~1 mm/yr of uplift over 2019-2023 on the island of Lichades and the
156 coastal land strip at Kammena Vourla (Wood et al., 2025). The shallowing of the sill has been
157 independently inferred through analysis of Pleistocene microfossil assemblages (Drinia et al.,
158 2014).

159 The main fluvial drainage of the rift system, the Sperchios River (Figure 2a) reflects a closed
160 sedimentary system throughout the Holocene with all transported sediment deposited in its
161 delta at the Maliakos Gulf (Pechlivanidou et al., 2018). During lowstand conditions, the river
162 likely drained through the Oreoi Channel (Figure 2a), although it is possible that drainage
163 fluctuated to the endorheic North Gulf of Evia Pleistocene lakes where deltaic packages are
164 resolved in seismic reflection data (Caroir et al., 2024; Van Andel and Perissoratis, 2006).

165 The Western Basin therefore likely alternated between a sedimentary sink and fluvial transfer
166 zone depending on prevailing base level and rate of accommodation generation, representing
167 a key contrast to the Gulf of Corinth where basin geometry is largely stable across lacustrine
168 and marine intervals (Gawthorpe et al., 2018).

169 3. Data and Methods

170 3.1 Seismic data and stratigraphic age model

171 Here, a high density, high resolution seismic reflection dataset across the Western Basin is
172 used to explore the sedimentary and tectonic development of the sub-basin in detail (WATER
173 I and II; Chanier and Gaullier, 2017; Chanier and Watremez, 2021; Figure 2b, Supplementary
174 Figure S5). The WATER surveys acquired ~1800 km of single channel sparker (50-300 J)
175 seismic profiles across the North Gulf of Evia, Oreoi Channel and Skopelos Basin. The
176 subset of 41 profiles used in this study are ca. 350 ms at maximum interpretable depth (~260

177 – 320 m) and data is typically interpreted to the first seabed multiple which obscures the
178 signal below. Seismic velocities are modelled as 1500 m/s for seawater and 1800 m/s for
179 depth conversions consistent with Caroir et al. (2024).

180 The WATER dataset has been studied previously to determine the regional structural anatomy
181 of the North Gulf of Evia and show the influence of strike-slip deformation at the western
182 termination of the North Anatolian Fault (Caroir et al., 2024). However, no pre-Holocene age
183 correlations have been made for the sedimentary stratigraphy in the offshore North Gulf of
184 Evia to date.

185 In this study, key seismic horizons (H1-H3) are identified in the dataset based on seismic
186 terminations including onlap relationships and erosive truncation (Catuneanu, 2002; Vail et
187 al., 1977). Between these horizons, seismic units (SU1-3) are defined and each unit is
188 characterised based on seismic attributes and geological significance, consistent with seismic
189 facies principles (Vail et al., 1977; Xu and Haq, 2022). Three-dimensional surfaces are
190 produced from the key seismic horizons to analyse spatial variability of sediment package
191 thickness across the gulf (Supplementary Figure S3) with isopachs for each SU calculated as
192 the difference between two surfaces.

193 Age estimates for the seismic horizons and units are derived from sequence stratigraphic
194 principles as unconformity-bounded sediment sequences at the margins of marine and
195 lacustrine systems preserve a record of relative base level change (Catuneanu, 2002; Vail et
196 al., 1977). In clastic systems at basin margins, deltas build up (i.e., aggrade) to prevailing
197 base level before growing outwards (i.e. prograde). When preserved in the geologic record,
198 these packages can be used to infer the sequential timing of local highstand and lowstand
199 periods (Catuneanu, 2002). For late-Quaternary sedimentation, well constrained eustatic sea

200 level curves (e.g., Spratt and Lisiecki, 2016) can be correlated to sequences of clinofolds to
201 generate age models for basin sedimentation (e.g., Bell et al., 2008; Lykousis et al., 2007a).

202 In the south of the Western Basin, a well-developed sequence of submerged clinofold
203 packages is found on seismic lines 107 and 049. These packages are used to establish age
204 estimates for seismic horizons through correlation to the sea level curve of Spratt and Lisiecki
205 (2016; Figure 3 and 4). Distinct clinofold package rollover points (i.e. topset to foreset
206 transition) are identified in seismic profiles and act as markers of past marine or lacustrine
207 relative base level in the gulf (Catuneanu, 2002). To establish if a clinofold package best
208 correlates to a highstand or lowstand interval, package geometry, apparent base level and
209 stratigraphic sequencing are considered (Catuneanu, 2002; Figure 3a and 3b). Packages are
210 defined as lowstands if they sit stratigraphically above a package with a higher indicated base
211 level or show an exaggerated sigmoidal geometry consistent with decreasing/low
212 accommodation (Figure 3a). Highstand sequences are defined if they build up to higher base
213 level than the underlying stratigraphic package (Figure 3b). Ages are provided with reference
214 to Marine Isotope Stages (MIS) and numeric values are assigned from the sea level stack of
215 Spratt and Lisiecki (2016).

216 Sill level is marked on base level diagrams at 40 m bsl and at a level consistent with an
217 uplifting sill at 0.1 mm/yr (i.e. 10 year period of 1 mm/yr uplift every 100 years; Wood et al.,
218 2025). Base levels below sill level are considered lacustrine and above are considered marine.

219 3.2 Identification and classification of normal faults

220 Offshore faults are identified in seismic reflection profiles and mapped across lines to
221 generate three-dimensional geometries. Structures are classified on the most recent key
222 seismic horizon (H1-H3) they offset, providing an estimate for most recent activity. Fault
223 throw is measured as the vertical offset of the key dated seismic horizons defined in the age

224 model across each structure and represents the maximum observable throw on each fault over
225 the given time interval. Throw rates are converted to slip rates with an assumed fault dip of
226 60-70°, consistent with measured fault planes on the Arkitsa Fault (Kranis, 2007). The full
227 fault database is summarised in more detail in the supplementary material (Figure S4; Table
228 S1 and S2).

229 Geological field work was conducted in April and October 2025 and included corroborating
230 previous works, refining onshore fault maps (Figure 2) and documenting evidence for
231 onshore uplift and young normal faulting within syn-rift stratigraphy (Supplementary Figure
232 S1).

233 4. Results

234 4.1 Seismic stratigraphy

235 Three major stratigraphic horizons are identified based on the observation of erosional
236 truncation, onlap terminations and significant changes in seismic character (H1, H2 and H3;).
237 These surfaces can be seen on the seismic profiles of Figure 3c and 4 and their character is
238 summarised in Figure 5.

239 Both H1 and H2 are highly erosive with overlying sediments commonly onlapping these
240 surfaces (Figure 3 and 4). These horizons each represent a depositional hiatus in the gulf,
241 representing extended periods of subaerial erosion when the North Gulf of Evia lake was
242 restricted to the deep Central basin (Van Andel and Perissoratis, 2006).

243 A significant change in seismic facies occurs across surface H3 (Figure 5). Younger,
244 overlying sediments are dominated by high amplitude reflectors and abundant clinoforms

245 while below H3, reflections are dominantly low amplitude punctuated by thin, high amplitude
246 packages (Figure 5 and 6). In places, overlying reflections onlap H3 (Figure 6b).

247 H1 to H3 bound three seismic units defined in Figure 4 (SU1-3). SU1 is found between the
248 seabed and H1. It is dominated by acoustically transparent fan deposits with a thin, high
249 amplitude drape elsewhere. SU1 is equivalent to the Upper Sequence of Caroir et al. (2024)
250 which is considered to represent Holocene sedimentation in that study. Shallow coring of this
251 seismic unit in the Central Basin has confirmed the Holocene age of these sediments (Drinia
252 et al., 2014; Sakellariou et al., 2007). The fan deposits that dominate the Western Basin are
253 derived from the Xerias River (Figure 2b; Van Andel and Perissoratis, 2006). The erosive
254 surface H1 therefore formed during the Last Glacial Maximum (MIS 2, ~12 ka).

255 SU2 is found between H1 and H2. It is highly variable in thickness, owing to erosive surfaces
256 at both the base (H2) and top (H1) of the unit and is characterised by abundant clinofolds
257 and onlapping reflectors (Figure 5 and 6). The reflections in the unit are typically high
258 amplitude which, based on seismic reflections and age correlations in the Gulf of Corinth
259 (e.g., Bell et al., 2008; Nixon et al., 2016), implies highstand conditions dominate
260 sedimentation during this time.

261 SU3, between H2 and H3, is similarly characterised by high amplitude reflections but tends
262 to be more laterally continuous and lower frequency than SU2 with fewer clinofolds (Figure
263 4). The unit, in deeper basin settings transitions from high amplitude to low amplitude while
264 in marginal depositional settings is nearly exclusively high amplitude with abundant internal
265 and external onlap relationships (Figure 6). SU3 unit is interpreted to represent highstand
266 sedimentation in a marginal sub-basin prior to subaerial exposure and the formation of H2.

267 4.2 Sequence stratigraphy

268 Sequence stratigraphy of deltaic clinoform packages in Figure 2 and 3 is used to attribute
269 ages to the seismic stratigraphy outlined above through correlation to expected base level in
270 the gulf. Within the sedimentary succession spanning H1 to H3 shown in Figure 2c and 2d,
271 nine distinct packages are identified. Based on the ordering of apparent relative base levels
272 and sequence geometries outlined in the schematic diagrams of Figure 2a and 2b, each
273 package is classified as a relative lowstand or highstand.

274 Seven lowstand indicators are interpreted between 98 and 135 m bsl (LS1-LS7). These
275 packages have cross-sectional widths of 200-600 m with heights of ~10-20 ms (~9-18 m).
276 LS1 and LS2 sit directly below H1 and indicate similar relative base levels of 98 and 109 m
277 respectively. As H1 very likely represents the base-Holocene surface (see section 4.1), these
278 clinoforms must have developed during moderately high lake level or brackish deposition in
279 MIS 3 at a base level between sill level and ~-80 m bsl (Figure 3d). Lake levels in both MIS
280 2 and MIS 4 were restricted to the Central Basin (Figure 1b; Van Andel and Perissoratis,
281 2006) so deltaic clinoforms are unlikely to have developed in this part of the Western Basin
282 during those intervals.

283 HS1, LS3, HS2 and LS4 follow in the stratigraphic sequence and compose the remaining
284 strata of SU2. HS1 and HS2 are interpreted as highstands as both aggradation of >40 m and
285 retreat towards the basin margin of ~1.2 km are resolved for these packages (see comparison
286 to Figure 3b). The rollover of HS1 is not imaged here so the apparent relative base level of
287 ~70 m bsl is considered a minimum possible value. LS3 (~118 m bsl) sits stratigraphically
288 above HS1 while LS4 (~114 m bsl) sits between HS1 and HS2 with the morphologies and
289 stratigraphic relationships of the two lowstand patterns indicative of a forced regression (see
290 comparison to Figure 2a). The downdip extension of the HS1 package bifurcates above and

291 below LS3 while the up-dip extent of this unit drapes HS2. Based on this sequencing, these
292 four packages are attributed to MIS 5 with HS2 being MIS 5e and the thin sediment drape
293 above this of HS1 likely being an amalgamation of MIS 5c and 5a. Significant local
294 subsidence between MIS 5e and 5c is required to allow this drape at a sea level that is
295 expected to be ~25 m lower than the extreme highstand of MIS 5e (Figure 3d). Based on
296 sequencing relationships to these highstands, LS3 is attributed to MIS 5b and LS4 assigned to
297 MIS 5d (Figure 3d).

298 Horizon H3 is located below this and, given its character as a strongly erosive surface, best
299 represents late-MIS6 when the Western Basin likely saw an extended period of subaerial
300 exposure following significant base level fall. Immediately below this surface is a package of
301 consistent deposition without a preserved associated clinoform package (Figure 3c). LS5
302 (~126 m bsl) is a laterally restricted clinoform package with an indicated relative base level
303 far below the underlying unit. It is therefore considered a lowstand interval (Figure 3a). LS6
304 (~125m bsl) is a narrow (~200m) clinoform set that builds up above the underlying package
305 (LS7; ~135 m bsl). However, it does not build up above horizon H3 and, given aggradation
306 from LS7 to LS6 is only ~10 m, both are considered lowstand packages. The stratigraphic
307 positioning of LS5 best fits a moderate lowstand during MIS 7 (MIS 7d) with overlying
308 sediment representing subsequent periods of higher sea level (i.e., MIS 7c-a). Finally, the two
309 closely related packages of LS6 and LS7 sit below a further interval of highstand
310 sedimentation (MIS 7e) and are best correlated to MIS 8.

311 Surface H3 marks the base of the interpreted clinoform packages in Figure 3c and 3d and,
312 given its nature as a cap to a high amplitude package marking a significant change in basin
313 sedimentation, is attributed to MIS 9e (Figure 3d). Correlation below H3 is uncertain due to
314 poor imaging in the seismic reflection dataset across the basin.

315 Figure 4a shows a well-developed sequence of clinoforms on an intersecting seismic profile
316 to Figure 3c (Figure 4b). All packages marked in Figure 4a are characterized as lowstand
317 intervals based on comparison to expected geometries (Figure 3a) with two packages
318 developed on the southeastern margin and four developed on the northwestern margin of a
319 small paleo-bathymetric depression. Stratigraphic sequencing here is comparable to Figure 3c
320 and all lowstand packages from Figure 3c are represented in this adjacent line, except LS2
321 which is not locally developed. Indicated base levels in Figure 3a are within 10% of
322 counterparts in Figure 3c for each resolved lowstand package except LS1 which has an
323 indicated depth of 17 m lower. This may imply heightened tectonic subsidence has occurred
324 at the southeastern end of this profile.

325 Based on this sequence stratigraphic model across both Figure 3 and 4, age estimates of H1-3
326 and SU1-3 are derived and attributed to the seismic stratigraphic architecture of Figure 5. In
327 short, H1 represents MIS 2 (~12 ka), H2 represents late-MIS 6 (~130 ka) and H3 represents
328 MIS 9e (~325 ka).

329 Key to the utility of the age model is that it can be mapped consistently across the Western
330 Basin and wider North Gulf of Evia. Figure 6 shows interpreted seismic profiles that span the
331 axial length of the Western Basin (Figure 6a) and cross the width of the study area (Figure
332 6b) with the age model of Figure 5 applied. The erosive nature of H1 and H2 and the acoustic
333 transparency of SU1 are well highlighted in Figure 5a and the onlapping relationships of H1-
334 3 are highlighted in the south of Figure 6b. The marked change in seismic expression beneath
335 horizon H3 is evident in across both profiles with a shift from high amplitude reflections
336 dominating above to low amplitude reflections below. Where apparent in Figure 6a,
337 clinoforms are restricted to SU2 and SU3 with indicated paleo-flow directions to the west. A
338 substantial (~2 km wide) clinoform package attributed to MIS 5e on line 229 also indicates

339 flow to the west. These flow directions are opposed to expected drainage to the southeast
340 based on modern depocenters (Figure 2).

341 4.3 Normal fault network

342 Application of the age model to develop a full tectonic evolutionary history of the Western
343 Basin demands a comprehensive map of offshore normal faults. Figure 7a and 7b show the
344 mapped offshore fault network from this study. 47 offshore fault segments are mapped with
345 lengths of 0.5 km to 12 km (see Supplementary Table S1 and S2). The structural fabric of the
346 offshore rift is characterised by dominantly E-W striking normal faults, following the axis of
347 the gulf (Figure 7). The density of sub-parallel normal faults across the width of the gulf
348 increases from west to east as 3 to 4 structures span the basin near Neochori and 16 faults are
349 mapped across the basin in the east (Figure 7a).

350 The base-Holocene surface (i.e. depth to H1 erosive surface) shown in Figure 7a and 7b
351 provides a clearer indication of Pleistocene depocenters of the basin than modern bathymetry
352 as the thick fan deposits from the Xerias River (Figure 2b) are stripped away. This surface
353 allows primary depocenter-controlling structures to be identified.

354 The fault network in Figure 7a is classified on most recent evident fault slip derived from the
355 youngest mapped horizon (H1-3) that they offset. Active faults (i.e. structures that offset H1
356 or the seabed) are depicted in red while faults that do not offset H1, H2 or H3 are considered
357 least active (grey). Figure 7b classifies each structure on the maximum resolved throw rate in
358 this study with separate rates calculated between each age-attributed horizon (Figure 5). Only
359 three faults exhibit throw rates of >0.75 mm/yr (F01, F08 and F10) with the highest throw
360 rate in the basin of ~ 3.75 mm/yr during the Holocene resolved for F01. Across all normal
361 faults, a median throw rate of 0.2 mm/yr is resolved.

362 The southeast of the Western Basin appears to be controlled by a single, east-northeast
363 striking ($\sim 260^\circ$) major normal fault zone (F01), here named the Kalypso Fault (from the
364 homonymous settlement west of Arkitsa; Figure 7a). At the eastern tip of the fault, spacing to
365 the onshore Arkitsa Fault segment is ~ 4 km with negligible spacing between the structures in
366 the west, particularly when the onshore continuation of the fault is considered (Figure 7a). A
367 potentially active normal fault had previously been inferred here based on the uplifted marine
368 terraces between the Arkitsa Fault and the modern coastline (Cundy et al., 2010;
369 Papanastassiou et al., 2014) and the fault is mapped as WB4 in the regional structural
370 analysis of Caroir et al. (2024). We find the onshore continuation at the western extent of the
371 Kalypso Fault to follow a topographic escarpment (Figure 7) where fault breccia with syn-rift
372 clasts and fault surfaces (79/025; dip/azimuth) are found (Supplementary Figure S1a).

373 The Central Graben, consisting of a major south dipping and north dipping normal fault (F10
374 and F08), is located along the axis of the gulf in the east of the study area (Figure 7). The
375 graben opens significantly to the east with a fault spacing of 200 m at the western tip of the
376 graben and > 2.5 km in the east (Figure 7a). The main faults of the graben appear to trend
377 further to the east to bound the deep Central Basin, suggesting the faults are a significant
378 modern bathymetric control in the gulf (c.f., Caroir et al., 2024). Slip is considerable on these
379 structures with Holocene throw rates of 0.9 mm/yr on the south dipping fault and 1.7 mm/yr
380 on the north dipping fault (Figure 7b).

381 The Asproneri Fault (F43) in the southwest generates a significant bathymetric escarpment
382 and appears to be a major control on accommodation generation in this area (Figure 6b and
383 7a). This structure is likely responsible for uplifted terraces in the hanging wall of the onshore
384 Agios Konstantinos Fault (Figure 2b; Supplementary Figure S1c). However, slip rates and
385 along-strike variation for this structure are poorly resolved due to the low density of seismic
386 profiles here (Figure 2b).

387 4.4 Syn-kinematic sedimentation

388 Integrating the sedimentary age model with the normal fault network in Figure 6 constructs a
389 picture of how major depocenters in the Western Basin have changed over time in response to
390 tectonic and environmental forcing. The syn-tectonic thickening of sediment packages into
391 the hanging wall of normal faults also provides an indication of timing, and rates, of fault
392 activity as hanging wall subsidence generates heightened accommodation space (e.g.,
393 Coveney et al., 2025; Gawthorpe and Leeder, 2000; Jackson et al., 2017). Figure 8 shows
394 sediment thickness isopachs of the three seismic units defined in Figure 5 (SU1-3) with the
395 thickening direction of each unit SU1-3 indicating the major structural controls on syn-rift
396 sedimentation at the time.

397 Figure 8a depicts a Holocene-only (SU1) isopach. In the west, sedimentation is dominated by
398 the ~50 m thick deposits of the Xerias Fan, while in the east, Holocene sedimentation is
399 thickest between the Kalypso Fault and a south-dipping series of faults ~3 km to the north
400 (F02, F03, F46 – Figure 7). Elsewhere in the Western Basin, a thin drape of SU1 caps the
401 underlying succession.

402 Figure 8b shows the thickness of SU2. This isopach also shows thickening towards the south
403 and the Kalypso Fault to a maximum thickness of ~30 m. Yet, preserved sediment thickness
404 of SU2 shows high variability due to an apparently wider spatial distribution of active
405 faulting during this time and erosion from the overlying H1 unconformity.

406 Figure 8c also shows significant thickening of SU3 to the south across both the east, towards
407 the Kalypso Fault, and west, towards the Asproneri Fault. Post-depositional faulting and
408 subaerial erosion during MIS 6 (H2) and MIS2 (H1) results in similarly high variability in
409 this isopach to Figure 8b.

410 Figure 8d shows a further isopach constructed from a pre-325 ka sediment package that is
411 only correlated across the deeper southeast of the study area due to poor imaging elsewhere.
412 In contrast to the overlying units, this package shows a thickening trend towards the north,
413 showing an inverted polarity of thickening. This implies that the major control on
414 accommodation generation in the depocenter during this interval was likely the south-dipping
415 fault of the Central Graben (Figure 8d and 9).

416 These sediment thickening trends are also depicted in profile in Figure 9. Here, SU1-3 show
417 significant syn-tectonic thickening into the immediate hanging wall of the Kalypso Fault.
418 SU3, for example thickens from 20 m to 54 m over 1.5 km towards the fault zone (Figure
419 9b). Packages below SU3, such as the pre-325 ka package mapped in the isopach of Figure
420 8d, maintain constant thickness into the Kalypso fault plane and instead thicken significantly
421 towards the Central Graben in the north (Figure 9a and 9b). This provides evidence that the
422 Kalypso Fault likely initiated to become the dominant syn-sedimentary control on the
423 Western Basin immediately prior to the deposition of SU3 (~325 ka).

424 Figure 9a also directly images the fault zone of the Kalypso Fault. From the offset of the ~12
425 ka surface across the Kalypso Fault (~45 m) in this profile, a maximum Holocene throw rate
426 of ~3.75 mm/yr is resolved (Figure 9b). Considering a long-term uplift to subsidence ratio of
427 1:2-3, consistent with normal faults in the Gulf of Corinth (e.g., Armijo et al., 1996; McNeill
428 et al., 2005; Nixon et al., 2024), the Kalypso Fault is likely responsible for ~0.9-1.3 mm/yr
429 footwall uplift. This is comparable to the estimated 1-1.5 mm/yr uplift rates derived for the
430 Arkitsa marine terraces in the immediate footwall of the Kalypso Fault, based on ^{14}C dating
431 of shelly fauna (Papanastassiou et al., 2014).

432 5. Discussion

433 5.1 Pleistocene evolution of the Western Basin

434 The seismic stratigraphic age model developed in this study (Figure 5) represents the first
435 pre-Holocene correlation proposed for the North Gulf of Evia. The age model is applicable
436 and consistent across the Western Basin (Figure 6) and allows both for the timing of fault
437 activity and the first estimates of Pleistocene slip rates of offshore normal faults in the North
438 Gulf of Evia to be derived (Figure 7). This has allowed several key events in the evolution of
439 the offshore Western Basin to be resolved as presented in the schematic evolutionary block
440 models of Figure 10a-c.

441 The initiation of the Kalypso Fault at ~325 ka, depicted in Figure 10a, represents a marked
442 change in the major depocenter geometry and structural control in the gulf with older
443 sedimentary units showing thickening towards the axial Central Graben (Figure 8d).

444 Following this, base level fall and subaerial exposure of the Western Basin resulted in
445 significant erosion (H2) and drainage reorganisation during late-MIS 6 (~130 ka; Figure 10b).
446 A similar significant regression occurred in the gulf during MIS 2, allowing the erosive H2
447 seismic surface to develop (Figure 5). During these extreme lowstand intervals, the studied
448 area represents a fluvial transfer zone for drainage towards the main sedimentary sink of the
449 rift system in the Central Basin (Figure 10b). The dominant westward paleo-flow direction of
450 clinoform packages in SU1 and SU2 of Figure 6a (opposite to modern drainage) suggests that
451 drainage reorganisation has been a common occurrence in the Western Basin throughout the
452 late-Pleistocene.

453 Subsequent flooding of the basin in the Holocene has promoted the rapid progradation of the
454 Xerias Delta, which has dominated Western Basin deposition over the Holocene (Figure 8a,
455 10c and 10d).

456 5.2 Age model comparison to the Gulf of Corinth

457 Comparing the age model presented in this study to similarly constructed age models for syn-
458 rift sedimentation in the Gulf of Corinth (e.g., Bell et al., 2008; Lykousis et al., 2007b; Nixon
459 et al., 2016) reveals a number of key similarities and differences between the rifts.

460 Like the offshore age models for basin sedimentation in the Gulf of Corinth (e.g., Bell et al.,
461 2008; Nixon et al., 2016) our age model is constrained by key seismic horizons representing
462 intervals of rapid environmental (i.e. base level) change. We define three key horizons (H1-3)
463 while seven key horizons are defined in the Gulf of Corinth age model of Nixon et al. (2016),
464 owing to deeper imaging of seismic reflection data there. H1 (~12 ka) and H2 (~130 ka) in
465 our study correlate with the upper two key horizons (H1 and H2) in the Gulf of Corinth
466 (Nixon et al., 2016). Horizon H3 from our study has a proposed age of ~325 ka and is
467 equivalent to H4 (~340 ka) in the model of Nixon et al. (2016) with the small age discrepancy
468 related to the position within the highstand package the horizon is placed.

469 The efficacy of the seismic age models of Nixon et al. (2016) and others have recently been
470 tested following International Ocean Discovery Program (IODP) drilling in the Gulf of
471 Corinth (McNeill et al., 2019; Nixon et al., 2024). This drilling has allowed the magneto- and
472 bio-stratigraphic dating of Corinth seismic horizons H1 (13 ka), H2 (129 ka) and H4 (335
473 ka), finding the proposed ages from the existing seismic stratigraphic model to all be within 5
474 ka (Nixon et al., 2024).

475 The seismic expression of the units however highlights several differences between the
476 Western Basin of the North Gulf of Evia and the Gulf of Corinth. Seismic units in the deep

477 basin settings in Corinth alternate between thick low amplitude packages, correlated to
478 lowstand lacustrine deposition, and thin high amplitude packages correlated to marine
479 deposition during highstands (Bell et al., 2008; Nixon et al., 2024). In contrast, the late-
480 Pleistocene seismic units in the North Gulf of Evia are near-universally characterised by high
481 amplitude reflections (Figure 5 and 6). This reflects the exaggerated sensitivity of the North
482 Gulf of Evia to sea level change. This sensitivity is due to a combination of the 40 m
483 Lichades Sill to the Aegean Sea (Figure 2b; 20 m shallower than the Rion Sill to the Gulf of
484 Corinth; McNeill et al., 2019) and the overall shallow bathymetry and palaeo-bathymetry of
485 the Western Basin (<120 m; Figure 7). As a result, sedimentation across much of the sub-
486 basin is restricted to interglacial highstands (e.g., MIS 5, 7 and 9) as lowstand Pleistocene
487 glacial lakes (e.g., MIS 2 and 6) were likely confined to the deep Central Basin (c.f., Van
488 Andel and Perissoratis, 2006). The distinct periods of subaerial exposure of the Western
489 Basin (Figure 10b) are also not widely seen across wide areas in the basins of the Gulf of
490 Corinth (Gawthorpe et al., 2018).

491 Reliable sedimentation rates are difficult to constrain in the Western Basin due to the strongly
492 developed H1 and H2 erosive surfaces (Figure 5). It is possible to deduce, however, that
493 sedimentation in the Western Basin is markedly slower than in the main depocenters of the
494 Gulf of Corinth. In the well-preserved seismic packages in the south of Figure 9, where
495 erosion appears to be minimal, sedimentation rates of 0.1-0.3 mm/yr are calculated for the
496 thickest sections of SU3 (20-54 m over ~195 kyrs) and 0.1-0.2 mm/yr (10-20 m over ~120
497 kyrs) for SU2. Despite these rates likely representing maxima in the Western Basin, they are
498 an order of magnitude slower than sedimentation over comparable time intervals in the main
499 depocenters of the Gulf of Corinth of 1-3 mm/yr (McNeill et al., 2019).

500 5.3 Normal fault migration in complex rifts

501 In the example of the western North Gulf of Evia, the overall structural anatomy of the rift
502 reflects an asymmetric graben with dominant structural control from the onshore Coastal
503 Faults and near-offshore Kalypso Fault (Figure 10d).

504 A trend of increasing recency of fault activity towards the Central Graben and Kalypso Fault
505 is resolved (Figure 7a). Faults on the northern margin of the basin have not generated
506 significant accommodation, nor do they show significant slip, during the deposition of SU1-3
507 with the major depocenters found to the south of the Central Graben (Figure 7b and 8). The
508 Kalypso Fault represents the northernmost migration of the fault systems of the southern
509 margin of the rift while migration from north has localised on the Central Graben (Figure 6b).
510 Holocene slip in the Central Graben is significant with ~ 2 mm/yr slip on the north-dipping
511 structure and ~ 1 mm/yr slip on the south-dipping fault. The south-dipping fault generated
512 significant hanging wall accommodation prior to ~ 325 ka (Figure 7d and 8).

513 Faults on the northern margin of the western basin appear to have migrated to broadly
514 parallel structures (Figure 7a). In contrast, the main migration event on the southern margin
515 from the Arkitsa Fault to Kalypso Fault has occurred across non-parallel faults with evolving
516 strike (Arkitsa = $\sim 280^\circ$; Kalypso = $\sim 260^\circ$; Figure 10d). This is interpreted to reflect the
517 geodynamic rotational influence on fault migration in the gulf. The western tip of both
518 Arkitsa and Kalypso segments join the Agios Konstantinos Fault at the same point resulting
519 in extremely tight fault spacing in this area (Figure 10d). It appears that this western tip has
520 acted as a rotational axis for this migration event.

521 The strike of the Kalypso Fault also reflects a comparable extension azimuth to the $\sim 70^\circ$
522 strike rupture plane resolved for the 2013 $M_w = 5.4$ Kallidromon earthquake sequence in the
523 same tectonic system (Ganas et al., 2014). This is consistent with measured strain from

524 geodetic studies which show present extension acts at an azimuth of $\sim 0 - 10^\circ$ (Briole et al.,
525 2021; Chousianitis et al., 2024; Sboras et al., 2025).

526 Activity on the Kalypso Fault initiated at ~ 325 ka, as inferred from a reverse in thickening
527 direction at this time towards the structure (Figure 8 and 9). The uplifted marine terrace
528 staircase in the footwall of the structure (Figure 10; Papanastassiou et al., 2014) implies that
529 footwall uplift of the Kalypso Fault has exceeded hanging wall subsidence of the Arkitsa
530 Fault over the late-Pleistocene. To achieve this, the Kalypso Fault has likely undergone fault
531 linkage to the other segments of the Coastal Fault System. This implies that the Arkitsa Fault
532 has seen a marked reduction in slip rate since the initiation of the Kalypso, in agreement with
533 previous work where late-Pleistocene slip on the Arkitsa Fault is reported to be as low as 0.7
534 mm/yr (Walker et al., 2010; Whittaker and Walker, 2015).

535 The Kalypso Fault has a segment length of ~ 12 km (Figure 7) and a linked length of ~ 30 km
536 to the Kammena Vourla Fault segment (Figure 2b). Our resolved throw rate of ~ 3.75 mm/yr
537 corresponds to a slip rate of $\sim 4.0-4.3$ mm/yr assuming fault dip of $60-70^\circ$ and is consistent
538 with the large normal fault (>10 km length) displacement-length scaling relationships of
539 Lathrop et al. (2022) given an initiation age of 325 ka. The Kalypso Fault presents significant
540 regional seismic hazard and is capable of hosting $M_w > 6$ earthquakes (Wells and
541 Coppersmith, 1994) and given its offshore location, also presents significant tsunami hazard
542 to the North Gulf of Evia. The Kalypso Fault could provide a potential source for the
543 currently unattributed tsunami-forming earthquake of 426 BCE (Freitag and Reicherter,
544 2019).

545 The establishment of the Kalypso Fault to become the dominant structural control on the
546 western rift occurred rapidly with significant throw accumulation and lateral growth
547 occurring within ~ 325 kyrs. Syn-kinematic thickening in Figure 9 appears to begin

548 immediately above H3 with no marked change in sediment thickening rate in the units above.
549 This highlights the rapid onset of slip on the Kalypso Fault to become dominant over
550 timescales less than 100 kyrs, likely close to 10 kyrs, and implies that normal fault migration
551 and establishment in young rift systems occur rapidly over these timescales.

552 Complex geodynamic settings are common in active rift systems (e.g., Brune et al., 2023;
553 Laó-Dávila et al., 2015; Mouslopoulou et al., 2007; Saria et al., 2014; Wallace et al., 2004)
554 and rifts preserved in the geological record (e.g., Duffy et al., 2015; Frizon de Lamotte et al.,
555 2015). Analogue and numerical models are used explore the influence of rotational strain on
556 rift development (e.g., Duclaux et al., 2020; Molnar et al., 2017; Schmid et al., 2022; Zwaan
557 et al., 2020; Zwaan and Schreurs, 2020) yet natural records of normal fault processes in these
558 settings remain underexamined. Processes such as the oblique fault migration and rapid slip
559 accumulation resolved here on the Kalypso Fault are likely not unique to the North Gulf of
560 Evia and occur across many active and failed rift systems. Adding to the quantity of studies
561 with strong temporal constraints in natural, complex rift settings will help to further develop a
562 detailed understanding of how faults and fault systems grow and migrate rapidly and interact
563 in non-simple tectonic regimes. In turn, this will serve to improve the accuracy and
564 applicability of numerical and analogue models of rift processes.

565 6 Conclusions

566 This study provides a high-resolution record of normal fault migration and basin evolution
567 during complex rifting from the western North Gulf of Evia, Central Greece. Here extension
568 is influenced by continental block rotation and strike-slip deformation from the North
569 Anatolian Fault (Figure 1 and 2) and as such, the rift offers a structural contrast to the nearby
570 orthogonal rifting in the Gulf of Corinth.

571 In this work:

- 572 - A consistent, syn-kinematic, seismic stratigraphic age model for the North Gulf of
573 Evia is defined for the first time, with three key mappable surfaces (H1-3) attributed
574 ages of ~12, ~130 and ~325 ka, based on a base-level correlation to subsurface
575 clinoform packages.
- 576 - Major syn-rift depocentres are located along the southern margin of the basin in the
577 hanging wall of the Kalypso Fault (~4 mm/yr slip rate) and additional significant syn-
578 kinematic control from the axial Central Graben (~1 – 2 mm/yr slip) is observed.
- 579 - Basinward migration of the active front of normal faulting is observed on both
580 margins of the rift system over the 10-100s kyr timescales resolved in this study.
581 Faults on the northern margin have migrated to sub-parallel structures (e.g., Central
582 Graben) while fault migration on the southern margin has occurred between structures
583 with evolving strike of ~20° (e.g., Kalypso Fault).
- 584 - The Kalypso Fault is found to exert dominant structural control on the basin currently.
585 This initiated at ~325 ka following an oblique fault migration event from the onshore
586 Arkitsa Fault. The Kalypso Fault became established rapidly as the dominant fault
587 over timescales of 10s kyrs and is linked to the existing, onshore Coastal Fault
588 System.

589 This study demonstrates the value of temporal constraints on syn-kinematic sedimentation
590 derived from high-resolution subsurface data to examine rapidly evolving fault and fault
591 system processes in complex settings.

592

593 Data Availability

594 The fault network produced from this study is available as a .kml file. Uninterpreted seismic
595 profiles presented in this study are available in the Supplementary Materials. Seismic
596 reflection data is available on request.

597 References

- 598 Agostini, A., Corti, G., Zeoli, A., Mulugeta, G., 2009. Evolution, pattern, and partitioning of
599 deformation during oblique continental rifting: Inferences from lithospheric-scale
600 centrifuge models. *Geochemistry, Geophysics, Geosystems* 10.
601 <https://doi.org/10.1029/2009GC002676>
- 602 Armijo, R., Meyer, B., King, G.C.P., Rigo, A., Papanastassiou, D., 1996. Quaternary
603 evolution of the Corinth Rift and its implications for the Late Cenozoic evolution of
604 the Aegean. *Geophysical Journal International* 126, 11–53.
605 <https://doi.org/10.1111/j.1365-246X.1996.tb05264.x>
- 606 Bell, R.E., Duclaux, G., Nixon, C.W., Gawthorpe, R.L., McNeill, L.C., 2017. High-angle, not
607 low-angle, normal faults dominate early rift extension in the Corinth Rift, central
608 Greece. *Geology* 46, 115–118. <https://doi.org/10.1130/G39560.1>
- 609 Bell, R.E., McNeill, L.C., Bull, J.M., Henstock, T.J., 2008. Evolution of the offshore western
610 Gulf of Corinth. *GSA Bulletin* 120, 156–178. <https://doi.org/10.1130/B26212.1>
- 611 Bell, R.E., McNeill, L.C., Bull, J.M., Henstock, T.J., Collier, R.E.L., Leeder, M.R., 2009.
612 Fault architecture, basin structure and evolution of the Gulf of Corinth Rift, central
613 Greece. *Basin Research* 21, 824–855. <https://doi.org/10.1111/j.1365-2117.2009.00401.x>
- 614
- 615 Bradley, K.E., Vassilakis, E., Hosa, A., Weiss, B.P., 2013. Segmentation of the Hellenides
616 recorded by Pliocene initiation of clockwise block rotation in Central Greece. *Earth
617 and Planetary Science Letters* 362, 6–19. <https://doi.org/10.1016/j.epsl.2012.11.043>
- 618 Briole, P., Ganas, A., Elias, P., Dimitrov, D., 2021. The GPS velocity field of the Aegean.
619 New observations, contribution of the earthquakes, crustal blocks model. *Geophysical
620 Journal International* 226, 468–492. <https://doi.org/10.1093/gji/ggab089>
- 621 Brune, S., 2014. Evolution of stress and fault patterns in oblique rift systems: 3-D numerical
622 lithospheric-scale experiments from rift to breakup. *Geochemistry, Geophysics,
623 Geosystems* 15, 3392–3415. <https://doi.org/10.1002/2014GC005446>
- 624 Brune, S., Corti, G., Ranalli, G., 2017. Controls of inherited lithospheric heterogeneity on rift
625 linkage: Numerical and analog models of interaction between the Kenyan and
626 Ethiopian rifts across the Turkana depression. *Tectonics* 36, 1767–1786.
627 <https://doi.org/10.1002/2017TC004739>
- 628 Brune, S., Kolawole, F., Olive, J.-A., Stamps, D.S., Buck, W.R., Buiter, S.J.H., Furman, T.,
629 Shillington, D.J., 2023. Geodynamics of continental rift initiation and evolution.
630 *Nature Reviews Earth & Environment* 4, 235–253. <https://doi.org/10.1038/s43017-023-00391-3>
- 631
- 632 Caroir, F., Chanier, F., Gaullier, V., Sakellariou, D., Bailleul, J., Maillard, A., Paquet, F.,
633 Watremez, L., Averbuch, O., Graveleau, F., Ferrière, J., 2024. Late Quaternary

634 deformation in the western extension of the North Anatolian Fault (North Evia,
635 Greece): Insights from very high-resolution seismic data (WATER surveys).
636 *Tectonophysics* 870, 230138–230138. <https://doi.org/10.1016/j.tecto.2023.230138>
637 Catuneanu, O., 2002. Sequence stratigraphy of clastic systems: concepts, merits, and pitfalls.
638 *Journal of African Earth Sciences* 35, 1–43. [https://doi.org/10.1016/S0899-5362\(02\)00004-0](https://doi.org/10.1016/S0899-5362(02)00004-0)
639
640 Chanier, F., Ferrière, J., Averbuch, O., Graveleau, F., Caroir, F., Gaullier, V., Watremez, L.,
641 2024. The Main Pelagonian Detachment (MPD): extensional reactivation of the
642 frontal thrust of the Internal Zones of the Hellenides (Greece). *Comptes Rendus.*
643 *Géoscience* 356, 207–229. <https://doi.org/10.5802/crgeos.255>
644 Chanier, F., Gaullier, V., 2017. WATER cruise, Téthys II R/V, Sismar.
645 <https://doi.org/10.17600/17009400>
646 Chanier, F., Watremez, L., 2021. WATER 2 cruise, RV Téthys II.
647 <https://doi.org/doi.org/10.17600/18001115>
648 Chousianitis, K., Sboras, S., Mouslopoulou, V., Chouliaras, G., Hristopoulos, D.T., 2024. The
649 Upper Crustal Deformation Field of Greece Inferred From GPS Data and Its
650 Correlation With Earthquake Occurrence. *Journal of Geophysical Research: Solid*
651 *Earth* 129, e2023JB028004. <https://doi.org/10.1029/2023JB028004>
652 Coveney, S.M., Bell, R.E., Wils, K., Lastras, G., Whittaker, A.C., 2025. The Early Evolution
653 of a Young Normal Fault in the Aysén Fjord, Chile. *Tectonics* 44, e2025TC008835.
654 <https://doi.org/10.1029/2025TC008835>
655 Cundy, A.B., Gaki-Papanastassiou, K., Papanastassiou, D., Maroukian, H., Frogley, M.R.,
656 Cane, T., 2010. Geological and geomorphological evidence of recent coastal uplift
657 along a major Hellenic normal fault system (the Kamena Vourla fault zone, NW
658 Evoikos Gulf, Greece). *Marine Geology* 271, 156–164.
659 <https://doi.org/10.1016/j.margeo.2010.02.009>
660 de Gelder, G., Fernández-Blanco, D., Melnick, D., Duclaux, G., Bell, R.E., Jara-Muñoz, J.,
661 Armijo, R., Lacassin, R., 2019. Lithospheric flexure and rheology determined by
662 climate cycle markers in the Corinth Rift. *Sci Rep* 9, 4260.
663 <https://doi.org/10.1038/s41598-018-36377-1>
664 Drinia, H., Antonarakou, A., Anastasakis, G., 2014. Late Quaternary micropalaeontological
665 record of a semi-enclosed marine basin, North Evoikos, central Aegean Sea.
666 *Quaternary International* 345, 18–31. <https://doi.org/10.1016/j.quaint.2014.04.011>
667 Duclaux, G., Huisman, R.S., May, D.A., 2020. Rotation, narrowing, and preferential
668 reactivation of brittle structures during oblique rifting. *Earth and Planetary Science*
669 *Letters* 531, 115952. <https://doi.org/10.1016/j.epsl.2019.115952>
670 Duffy, O.B., Bell, R.E., Jackson, C.A.-L., Gawthorpe, R.L., Whipp, P.S., 2015. Fault growth
671 and interactions in a multiphase rift fault network: Horda Platform, Norwegian North
672 Sea. *Journal of Structural Geology* 80, 99–119.
673 <https://doi.org/10.1016/j.jsg.2015.08.015>
674 Feng, Y., Jiang, S., Hu, S., Li, S., Lin, C., Xie, X., 2016. Sequence stratigraphy and
675 importance of syndepositional structural slope-break for architecture of Paleogene
676 syn-rift lacustrine strata, Bohai Bay Basin, E. China. *Marine and Petroleum Geology*
677 69, 183–204. <https://doi.org/10.1016/j.marpetgeo.2015.10.013>
678 Fernández-Blanco, D., de Gelder, G., Lacassin, R., Armijo, R., 2019. A new crustal fault
679 formed the modern Corinth Rift. *Earth-Science Reviews* 199, 102919.
680 <https://doi.org/10.1016/j.earscirev.2019.102919>
681 Ford, M., Hemelsdaël, R., Mancini, M., Palyvos, N., 2017. Rift migration and lateral
682 propagation: evolution of normal faults and sediment-routing systems of the western

683 Corinth rift (Greece). Geological Society, London, Special Publications 439, 131–168.
684 <https://doi.org/10.1144/SP439.15>

685 Freitag, K., Reicherter, K., 2019. The earthquake and tsunami of 426 BC in Greece:
686 observations by Thucydides and contextual interpretations. *Zeitschrift für*
687 *Geomorphologie, Supplementary Issues* 62, 47–62.
688 https://doi.org/10.1127/zfg_suppl/2019/0625

689 Frizon de Lamotte, D., Fourdan, B., Leleu, S., Leparmentier, F., de Clarens, P., 2015. Style of
690 rifting and the stages of Pangea breakup. *Tectonics* 34, 1009–1029.
691 <https://doi.org/10.1002/2014TC003760>

692 Galanakis, D., Sboras, S., Sakellariou, D., Pavlides, S., Iordanidou, K., Georgiou, C., Ganas,
693 A., Koukouvelas, I., Kranis, C., Lalechos, S., Rondoyanni, T., Lekkas, E., 2025. The
694 Hellenic DataBase of Active Faults (HeDBAF): a new, national geodatabase of active
695 faults for the broader Greek territory. Presented at the EGU 2025, Copernicus
696 Meetings, Vienna. <https://doi.org/10.5194/egusphere-egu25-9230>

697 Ganas, A., Karastathis, V., Moshou, A., Valkaniotis, S., Mouzakiotis, E., Papathanassiou, G.,
698 2014. Aftershock relocation and frequency–size distribution, stress inversion and
699 seismotectonic setting of the 7 August 2013 M=5.4 earthquake in Kallidromon
700 Mountain, central Greece. *Tectonophysics* 617, 101–113.
701 <https://doi.org/10.1016/j.tecto.2014.01.022>

702 Ganas, A., Mouzakiotis, E., Moshou, A., Karastathis, V., 2016. Left-lateral shear inside the
703 North Gulf of Evia Rift, Central Greece, evidenced by relocated earthquake sequences
704 and moment tensor inversion. *Tectonophysics* 682, 237–248.
705 <https://doi.org/10.1016/j.tecto.2016.05.031>

706 Ganas, A., Oikonomou, I.A., Tsimi, C., 2013. NOAfaults: a digital database for active faults
707 in Greece. *Bulletin of the Geological Society of Greece* 47, 518–530.
708 <https://doi.org/10.12681/bgsg.11079>

709 Ganas, A., Roberts, G.P., Memou, T., 1998. Segment boundaries, the 1894 ruptures and strain
710 patterns along the Atalanti Fault, Central Greece. *Journal of Geodynamics* 26, 461–
711 486. [https://doi.org/10.1016/S0264-3707\(97\)00066-5](https://doi.org/10.1016/S0264-3707(97)00066-5)

712 Gawthorpe, R.L., Andrews, J.E., Collier, R.E.L., Ford, M., Henstra, G.A., Kranis, H., Leeder,
713 M.R., Muravchik, M., Skourtsos, E., 2017. Building up or out? Disparate sequence
714 architectures along an active rift margin—Corinth rift, Greece. *Geology* 45, 1111–
715 1114. <https://doi.org/10.1130/G39660.1>

716 Gawthorpe, R.L., Leeder, M.R., 2000. Tectono-sedimentary evolution of active extensional
717 basins. *Basin Research* 12, 195–218. [https://doi.org/10.1111/j.1365-](https://doi.org/10.1111/j.1365-2117.2000.00121.x)
718 [2117.2000.00121.x](https://doi.org/10.1111/j.1365-2117.2000.00121.x)

719 Gawthorpe, R.L., Leeder, M.R., Kranis, H., Skourtsos, E., Andrews, J.E., Henstra, G.A.,
720 Mack, G.H., Muravchik, M., Turner, J.A., Stamatakis, M., 2018. Tectono-sedimentary
721 evolution of the Plio-Pleistocene Corinth rift, Greece. *Basin Research* 30, 448–479.
722 <https://doi.org/10.1111/bre.12260>

723 Goldsworthy, M., Jackson, J., Haines, J., 2002. The continuity of active fault systems in
724 Greece. *Geophysical Journal International* 148, 596–618.
725 <https://doi.org/10.1046/j.1365-246X.2002.01609.x>

726 Hatzfeld, D., Ziazia, M., Kementzetzidou, D., Hatzidimitriou, P., Panagiotopoulos, D.,
727 Makropoulos, K., Papadimitriou, P., Deschamps, A., 1999. Microseismicity and focal
728 mechanisms at the western termination of the North Anatolian Fault and their
729 implications for continental tectonics. *Geophysical Journal International* 137, 891–
730 908. <https://doi.org/10.1046/j.1365-246x.1999.00851.x>

731 IGME, 2006. Geological Map of Greece, 1:50,000 Scale (Pelasgia sheet, 2006; Istaia sheet,
732 1984; Elatia sheet, 1967; Atalanti sheet, 1965).

733 Jackson, Christopher A.-L., Bell, R.E., Rotevatn, A., Tvedt, A.B.M., 2017. Techniques to
734 determine the kinematics of synsedimentary normal faults and implications for fault
735 growth models, in: Childs, C., Holdsworth, R.E., Jackson, C. A.-L., Manzocchi, T.,
736 Walsh, J.J., Yielding, G. (Eds.), *The Geometry and Growth of Normal Faults*. The
737 Geological Society of London, p. 0. <https://doi.org/10.1144/SP439.22>

738 Jolivet, L., Faccenna, C., Huet, B., Labrousse, L., Le Pourhiet, L., Lacombe, O., Lecomte, E.,
739 Burov, E., Denèle, Y., Brun, J.-P., Philippon, M., Paul, A., Salaün, G., Karabulut, H.,
740 Piromallo, C., Monié, P., Gueydan, F., Okay, A.I., Oberhänsli, R., Pourteau, A.,
741 Augier, R., Gadenne, L., Driussi, O., 2013. Aegean tectonics: Strain localisation, slab
742 tearing and trench retreat. *Tectonophysics, The Aegean: a natural laboratory for*
743 *tectonics - Neotectonics* 597–598, 1–33. <https://doi.org/10.1016/j.tecto.2012.06.011>

744 Jourdon, A., Le Pourhiet, L., Mouthereau, F., May, D., 2020. Modes of Propagation of
745 Continental Breakup and Associated Oblique Rift Structures. *Journal of Geophysical*
746 *Research: Solid Earth* 125, e2020JB019906. <https://doi.org/10.1029/2020JB019906>

747 Kranis, H., 2007. Neotectonic Basin Evolution in Central-Eastern Mainland Greece: An
748 Overview. *Bulletin of the Geological Society of Greece* 40, 360–373.
749 <https://doi.org/10.12681/bgsg.16621>

750 Kranis, H., Palyvos, N., Livaditis, G., Maroukian, H., 2001. The Hyambolis zone:
751 geomorphological and tectonic evidence of a transverse structure in Lokris (Central
752 Greece). *Bulletin of the Geological Society of Greece* 34, 251–251.
753 <https://doi.org/10.12681/bgsg.17020>

754 Laó-Dávila, D.A., Al-Salmi, H.S., Abdelsalam, M.G., Atekwana, E.A., 2015. Hierarchical
755 segmentation of the Malawi Rift: The influence of inherited lithospheric heterogeneity
756 and kinematics in the evolution of continental rifts. *Tectonics* 34, 2399–2417.
757 <https://doi.org/10.1002/2015TC003953>

758 Lathrop, B.A., Jackson, C. a.-L., Bell, R.E., Rotevatn, A., 2022. Displacement/Length Scaling
759 Relationships for Normal Faults; a Review, Critique, and Revised Compilation. *Front.*
760 *Earth Sci.* 10. <https://doi.org/10.3389/feart.2022.907543>

761 Leeder, M.R., Mack, G.H., Brasier, A.T., Parrish, R.R., McIntosh, W.C., Andrews, J.E.,
762 Duermeijer, C.E., 2008. Late-Pliocene timing of Corinth (Greece) rift-margin fault
763 migration. *Earth and Planetary Science Letters* 274, 132–141.
764 <https://doi.org/10.1016/j.epsl.2008.07.006>

765 Lykousis, V., Sakellariou, D., Moretti, I., Kaberi, H., 2007a. Late Quaternary basin evolution
766 of the Gulf of Corinth: Sequence stratigraphy, sedimentation, fault–slip and
767 subsidence rates. *Tectonophysics, Deep structure, fault arrays and surface processes*
768 *within an active graben: The Gulf of Corinth* 440, 29–51.
769 <https://doi.org/10.1016/j.tecto.2006.11.007>

770 Lykousis, V., Sakellariou, D., Moretti, I., Kaberi, H., 2007b. Late Quaternary basin evolution
771 of the Gulf of Corinth: Sequence stratigraphy, sedimentation, fault–slip and
772 subsidence rates. *Tectonophysics* 440, 29–51.
773 <https://doi.org/10.1016/j.tecto.2006.11.007>

774 McNeill, L.C., Collier, R.E.Ll., De Martini, P.M., Pantosti, D., D’Addezio, G., 2005. Recent
775 history of the Eastern Eliki Fault, Gulf of Corinth: geomorphology, palaeoseismology
776 and impact on palaeoenvironments. *Geophysical Journal International* 161, 154–166.
777 <https://doi.org/10.1111/j.1365-246X.2005.02559.x>

778 McNeill, L.C., Shillington, D.J., Carter, G.D.O., Everest, J.D., Gawthorpe, R.L., Miller, C.,
779 Phillips, M.P., Collier, R.E.Ll., Cvetkoska, A., De Gelder, G., Diz, P., Doan, M.-L.,
780 Ford, M., Geraga, M., Gillespie, J., Hemelsdaël, R., Herrero-Bervera, E., Ismaiel, M.,
781 Janikian, L., Kouli, K., Le Ber, E., Li, S., Maffione, M., Mahoney, C., Machlus, M.L.,
782 Michas, G., Nixon, C.W., Oflaz, S.A., Omale, A.P., Panagiotopoulos, K.,

783 Pechlivanidou, S., Sauer, S., Seguin, J., Sergiou, S., Zakharova, N.V., Green, S., 2019.
784 High-resolution record reveals climate-driven environmental and sedimentary
785 changes in an active rift. *Scientific Reports* 9, 3116–3116.
786 <https://doi.org/10.1038/s41598-019-40022-w>

787 Mildon, Z.K., Diercks, M., Roberts, G.P., Faure Walker, J.P., Ganas, A., Papanikolaou, I.,
788 Sakas, V., Robertson, J., Sgambato, C., Mitchell, S., 2024. Transient Aseismic Vertical
789 Deformation Across the Steeply-Dipping Pisia-Skinos Normal Fault (Gulf of Corinth,
790 Greece). *Tectonics* 43, e2024TC008276-e2024TC008276.
791 <https://doi.org/10.1029/2024TC008276>

792 Molnar, N.E., Cruden, A.R., Betts, P.G., 2017. Interactions between propagating rotational
793 rifts and linear rheological heterogeneities: Insights from three-dimensional laboratory
794 experiments. *Tectonics* 36, 420–443. <https://doi.org/10.1002/2016TC004447>

795 Mouslopoulou, V., Nicol, A., Little, T.A., Walsh, J.J., 2007. Displacement transfer between
796 intersecting regional strike-slip and extensional fault systems. *Journal of Structural*
797 *Geology* 29, 100–116. <https://doi.org/10.1016/j.jsg.2006.08.002>

798 Nixon, C.W., McNeill, L.C., Bull, J.M., Bell, R.E., Gawthorpe, R.L., Henstock, T.J.,
799 Christodoulou, D., Ford, M., Taylor, B., Sakellariou, D., Ferentinos, G.,
800 Papatheodorou, G., Leeder, M.R., Collier, R.E.L.I., Goodliffe, A.M., Sachpazi, M.,
801 Kranis, H., 2016. Rapid spatiotemporal variations in rift structure during development
802 of the Corinth Rift, central Greece. *Tectonics* 35, 1225–1248.
803 <https://doi.org/10.1002/2015TC004026>

804 Nixon, C.W., McNeill, L.C., Gawthorpe, R.L., Shillington, D.J., Michas, G., Bell, R.E.,
805 Moyle, A., Ford, M., Zakharova, N.V., Bull, J.M., de Gelder, G., 2024. Increasing
806 fault slip rates within the Corinth Rift, Greece: A rapidly localising active rift fault
807 network. *Earth and Planetary Science Letters* 636, 118716.
808 <https://doi.org/10.1016/j.epsl.2024.118716>

809 Palyvos, N., Bantekas, I., Kranis, H., 2006. Transverse fault zones of subtle geomorphic
810 signature in northern Evia island (central Greece extensional province): An
811 introduction to the Quaternary Nileas graben. *Geomorphology* 76, 363–374.
812 <https://doi.org/10.1016/j.geomorph.2005.12.002>

813 Pantosti, D., De Martini, P.M., Papanastassiou, D., Lemeille, F., Palyvos, N., Stavrakakis, G.,
814 2004. Paleoseismological Trenching across the Atalanti Fault (Central Greece):
815 Evidence for the Ancestors of the 1894 Earthquake during the Middle Ages and
816 Roman Times. *Bulletin of the Seismological Society of America* 94, 531–549.
817 <https://doi.org/10.1785/0120020207>

818 Papanastassiou, D., Cundy, A.B., Gaki-Papanastassiou, K., Frogley, M.R., Tsanakas, K.,
819 Maroukian, H., 2014. The Uplifted Terraces of the Arkitsa Region, NW Evoikos Gulf,
820 Greece: A Result of Combined Tectonic and Volcanic Processes? *The Journal of*
821 *Geology* 122, 397–410. <https://doi.org/10.1086/676595>

822 Papanikolaou, D., 2021. The Geology of Greece. <https://doi.org/10.1007/978-3-030-60731-9>

823 Papanikolaou, D., Royden, L.H., 2007. Disruption of the Hellenic arc: Late Miocene
824 extensional detachment faults and steep Pliocene-Quaternary normal faults—Or what
825 happened at Corinth? *Tectonics* 26. <https://doi.org/10.1029/2006TC002007>

826 Pechlivanidou, S., Cowie, P.A., Hannisdal, B., Whittaker, A.C., Gawthorpe, R.L., Pennos, C.,
827 Riiser, O.S., 2018. Source-to-sink analysis in an active extensional setting: Holocene
828 erosion and deposition in the Sperchios rift, central Greece. *Basin Research* 30, 522–
829 543. <https://doi.org/10.1111/bre.12263>

830 Phillips, T.B., Fazlikhani, H., Gawthorpe, R.L., Fossen, H., Jackson, C.A.-L., Bell, R.E.,
831 Faleide, J.I., Rotevatn, A., 2019. The Influence of Structural Inheritance and

832 Multiphase Extension on Rift Development, the Northern North Sea. *Tectonics* 38,
833 4099–4126. <https://doi.org/10.1029/2019TC005756>

834 Pirazzoli, P.A., Stiros, S.C., Arnold, M., Laborel, J., Laborel-Deguen, F., 1999. Late holocene
835 coseismic vertical displacements and tsunami deposits near Kynos, Gulf of Euboea,
836 Central Greece. *Physics and Chemistry of the Earth, Part A: Solid Earth and Geodesy*
837 24, 361–367. [https://doi.org/10.1016/S1464-1895\(99\)00042-3](https://doi.org/10.1016/S1464-1895(99)00042-3)

838 Roberts, G.P., Ganas, A., 2000. Fault-slip directions in central and southern Greece measured
839 from striated and corrugated fault planes: Comparison with focal mechanism and
840 geodetic data. *Journal of Geophysical Research: Solid Earth* 105, 23443–23462.
841 <https://doi.org/10.1029/1999JB900440>

842 Roberts, S., Jackson, J., 1991. Active normal faulting in central Greece: an overview.
843 Geological Society, London, Special Publications 56, 125–142.
844 <https://doi.org/10.1144/GSL.SP.1991.056.01.09>

845 Sakellariou, D., Rousakis, G., Kaberi, H., Kapsimalis, V., Georgiou, P., Kanellopoulos, Th.,
846 Lykousis, V., 2007. Tectono-Sedimentary Structure and Late Quaternary Evolution Of
847 The North Evia Gulf Basin, Central Greece: Preliminary Results. *Bulletin of the*
848 *Geological Society of Greece* 40, 451–462. <https://doi.org/10.12681/bgsg.16644>

849 Saria, E., Calais, E., Stamps, D.S., Delvaux, D., Hartnady, C.J.H., 2014. Present-day
850 kinematics of the East African Rift. *Journal of Geophysical Research: Solid Earth*
851 119, 3584–3600. <https://doi.org/10.1002/2013JB010901>

852 Sboras, S., Mouzakiotis, E., Chousianitis, K., Karastathis, V., Evangelidis, C.P., Lazos, I.,
853 Papageorgiou, A., Liakopoulos, S., Iordanidou, K., 2025. Where does the active North
854 Aegean Sea shear stop? Geodynamic and seismotectonic implications from recent
855 strike-slip earthquake occurrences and GPS-based geodetic analysis in Euboea,
856 Phthiotis and Boeotia, Central Greece. *Tectonophysics* 914, 230917.
857 <https://doi.org/10.1016/j.tecto.2025.230917>

858 Schmid, T.C., Schreurs, G., Adam, J., 2022. Characteristics of continental rifting in rotational
859 systems: New findings from spatiotemporal high resolution quantified crustal scale
860 analogue models. *Tectonophysics* 822, 229174.
861 <https://doi.org/10.1016/j.tecto.2021.229174>

862 Spratt, R.M., Lisiecki, L.E., 2016. A Late Pleistocene sea level stack. *Climate of the Past* 12,
863 1079–1092. <https://doi.org/10.5194/cp-12-1079-2016>

864 Vail, P.R., Mitchum, R.M., Jr., Thompson, S., III, 1977. Seismic Stratigraphy and Global
865 Changes of Sea Level, Part 4: Global Cycles of Relative Changes of Sea Level, in:
866 Payton, C.E. (Ed.), *Seismic Stratigraphy — Applications to Hydrocarbon Exploration*.
867 American Association of Petroleum Geologists, p. 0.
868 <https://doi.org/10.1306/M26490C6>

869 Van Andel, T H, Perissoratis, C., 2006. Late Quaternary depositional history of the North
870 Evvoikos Gulf, Aegean Sea, Greece. *Marine Geology* 232, 157–172.
871 <https://doi.org/10.1016/j.margeo.2006.07.004>

872 Van Andel, T. H., Perissoratis, C., 2006. Late Quaternary depositional history of the North
873 Evvoikos Gulf, Aegean Sea, Greece. *Marine Geology* 232, 157–172.
874 <https://doi.org/10.1016/j.margeo.2006.07.004>

875 Walker, R.T., Claisse, S., Telfer, M., Nissen, E., England, P., Bryant, C., Bailey, R., 2010.
876 Preliminary estimate of Holocene slip rate on active normal faults bounding the
877 southern coast of the Gulf of Evia, central Greece. *Geosphere* 6, 583–593.
878 <https://doi.org/10.1130/GES00542.1>

879 Wallace, L.M., Beavan, J., McCaffrey, R., Darby, D., 2004. Subduction zone coupling and
880 tectonic block rotations in the North Island, New Zealand. *Journal of Geophysical*
881 *Research: Solid Earth* 109. <https://doi.org/10.1029/2004JB003241>

882 Watkins, S.E., Whittaker, A.C., Bell, R.E., McNeill, L.C., Gawthorpe, R.L., Brooke, S.A.S.,
883 Nixon, C.W., 2018. Are landscapes buffered to high-frequency climate change? A
884 comparison of sediment fluxes and depositional volumes in the Corinth Rift, central
885 Greece, over the past 130 k.y. *GSA Bulletin* 131, 372–388.
886 <https://doi.org/10.1130/B31953.1>

887 Wells, D.L., Coppersmith, K.J., 1994. New empirical relationships among magnitude, rupture
888 length, rupture width, rupture area, and surface displacement. *Bulletin of the*
889 *Seismological Society of America* 84, 974–1002.
890 <https://doi.org/10.1785/BSSA0840040974>

891 Whittaker, A.C., Walker, A.S., 2015. Geomorphic constraints on fault throw rates and linkage
892 times: Examples from the Northern Gulf of Evia, Greece. *Journal of Geophysical*
893 *Research: Earth Surface* 120, 137–158. <https://doi.org/10.1002/2014JF003318>

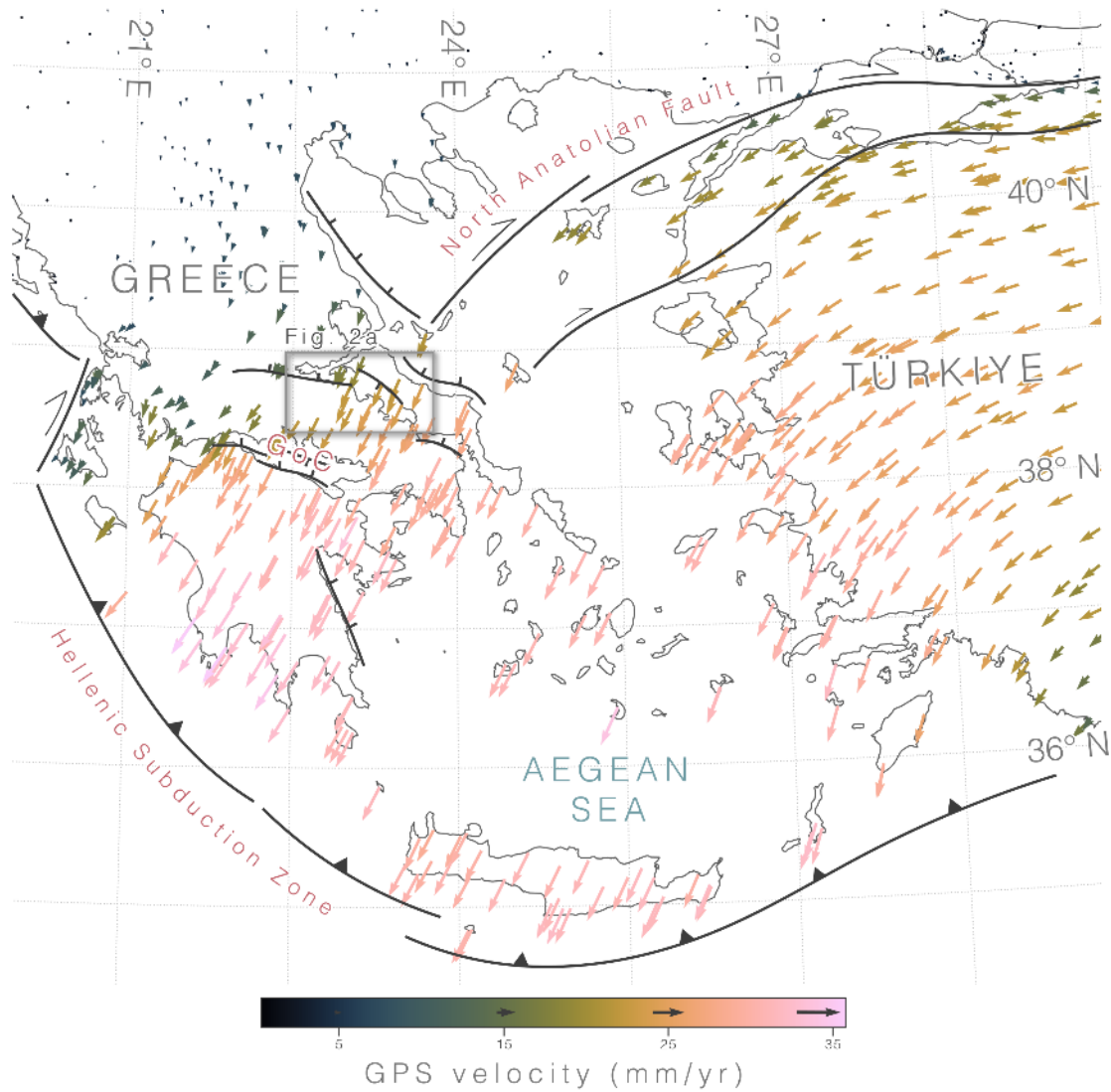
894 Wood, J., Whittaker, A.C., Bell, R.E., Coveney, S.M., Kranis, H.D., 2025. Resolving
895 Coseismic and Aseismic Normal Fault Slip Behaviors From InSAR Time Series of the
896 European Ground Motion Service (EGMS). *Tectonics* 44, e2025TC008904.
897 <https://doi.org/10.1029/2025TC008904>

898 Xu, G., Haq, B.U., 2022. Seismic facies analysis: Past, present and future. *Earth-Science*
899 *Reviews* 224, 103876. <https://doi.org/10.1016/j.earscirev.2021.103876>

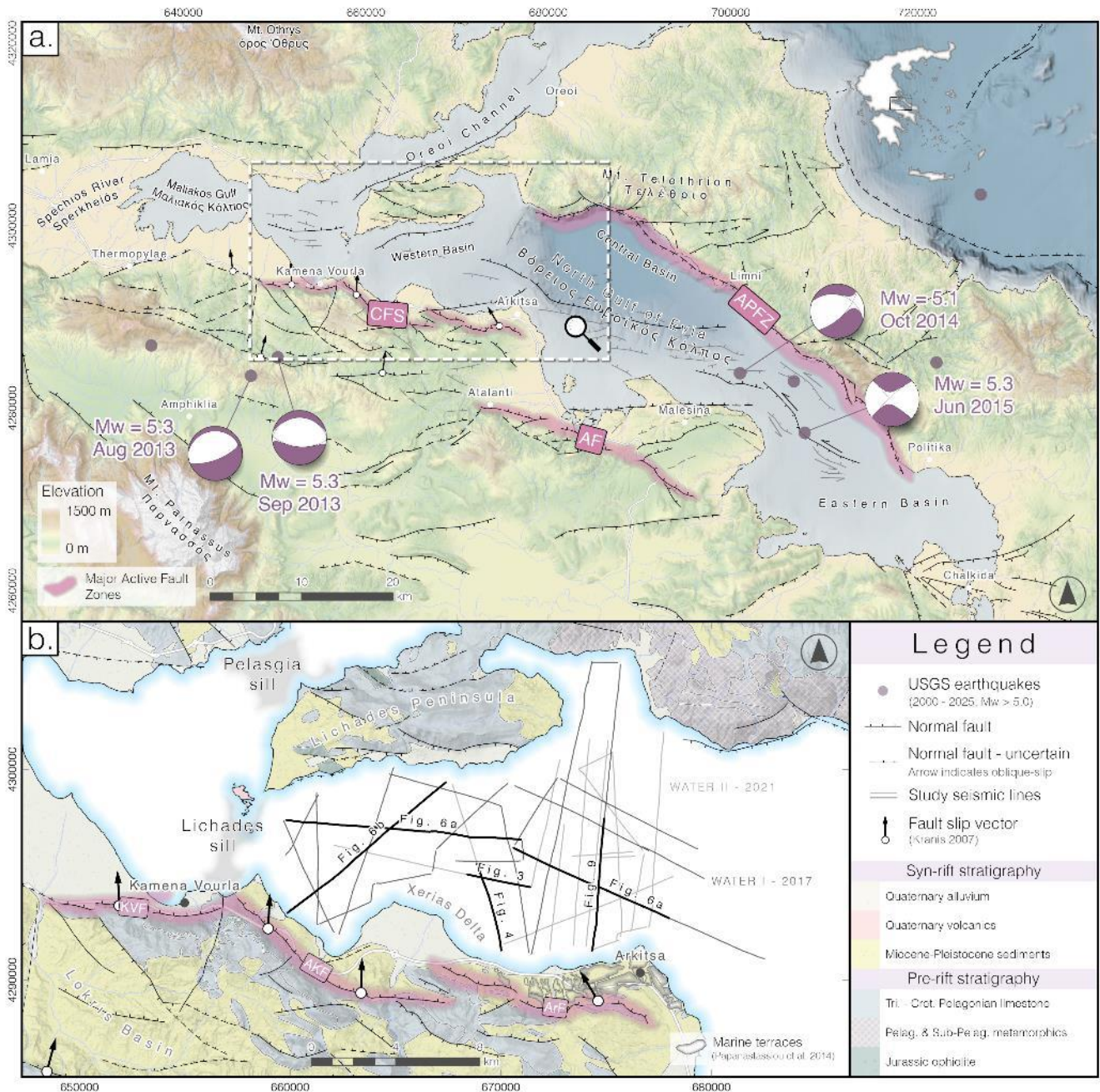
900 Zwaan, F., Schreurs, G., 2020. Rift segment interaction in orthogonal and rotational extension
901 experiments: Implications for the large-scale development of rift systems. *Journal of*
902 *Structural Geology* 140, 104119. <https://doi.org/10.1016/j.jsg.2020.104119>

903 Zwaan, F., Schreurs, G., Rosenau, M., 2020. Rift propagation in rotational versus orthogonal
904 extension: Insights from 4D analogue models. *Journal of Structural Geology* 135,
905 103946. <https://doi.org/10.1016/j.jsg.2019.103946>

906

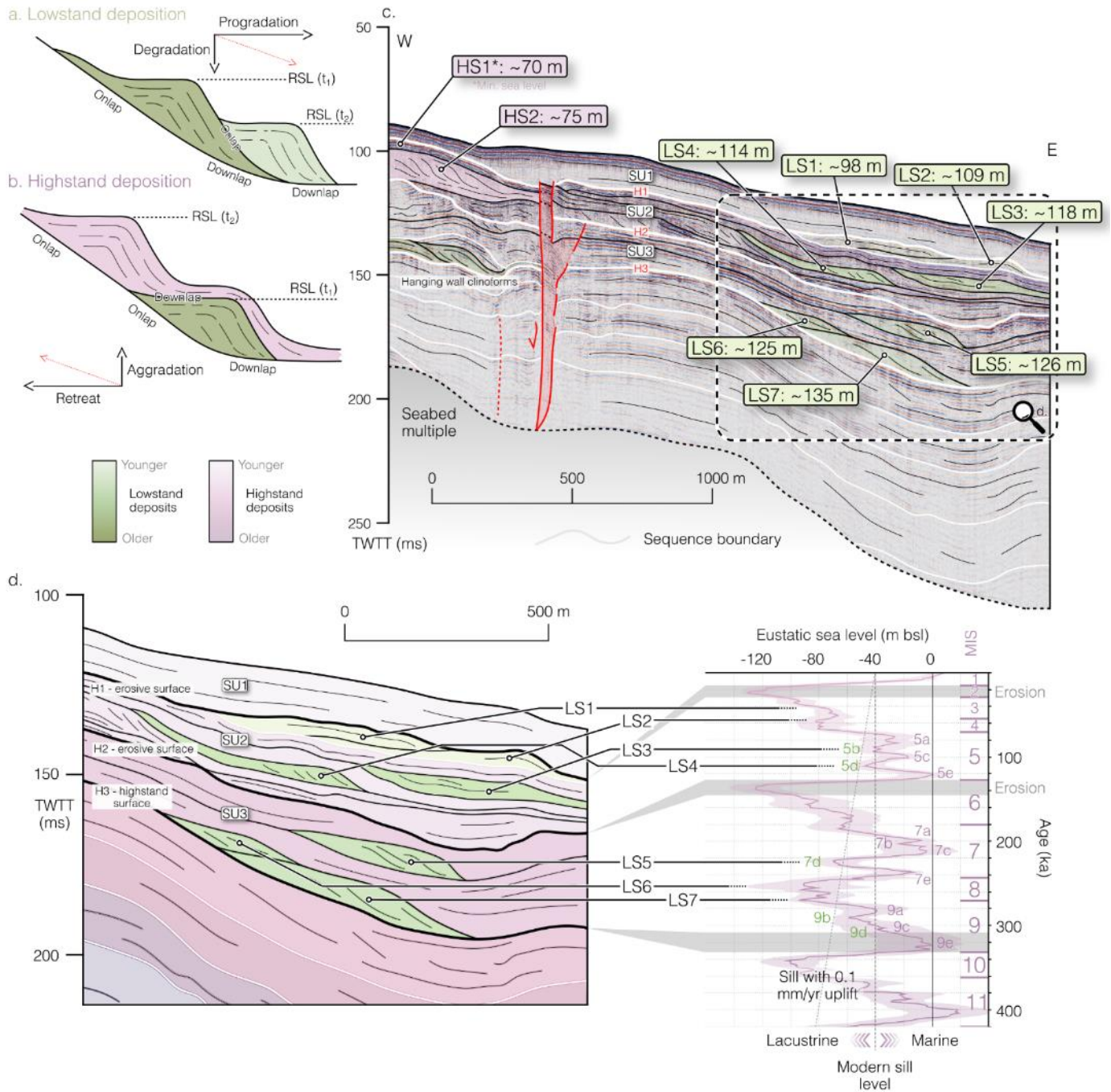


908 **Figure 1:** Tectonic overview of the Aegean domain with GPS velocity field of the Eastern
909 Mediterranean relative to stable Eurasia from Chousianitis et al. (2024). GoC = Gulf of
910 Corinth. Major fault zones after (Papanikolaou and Royden, 2007).



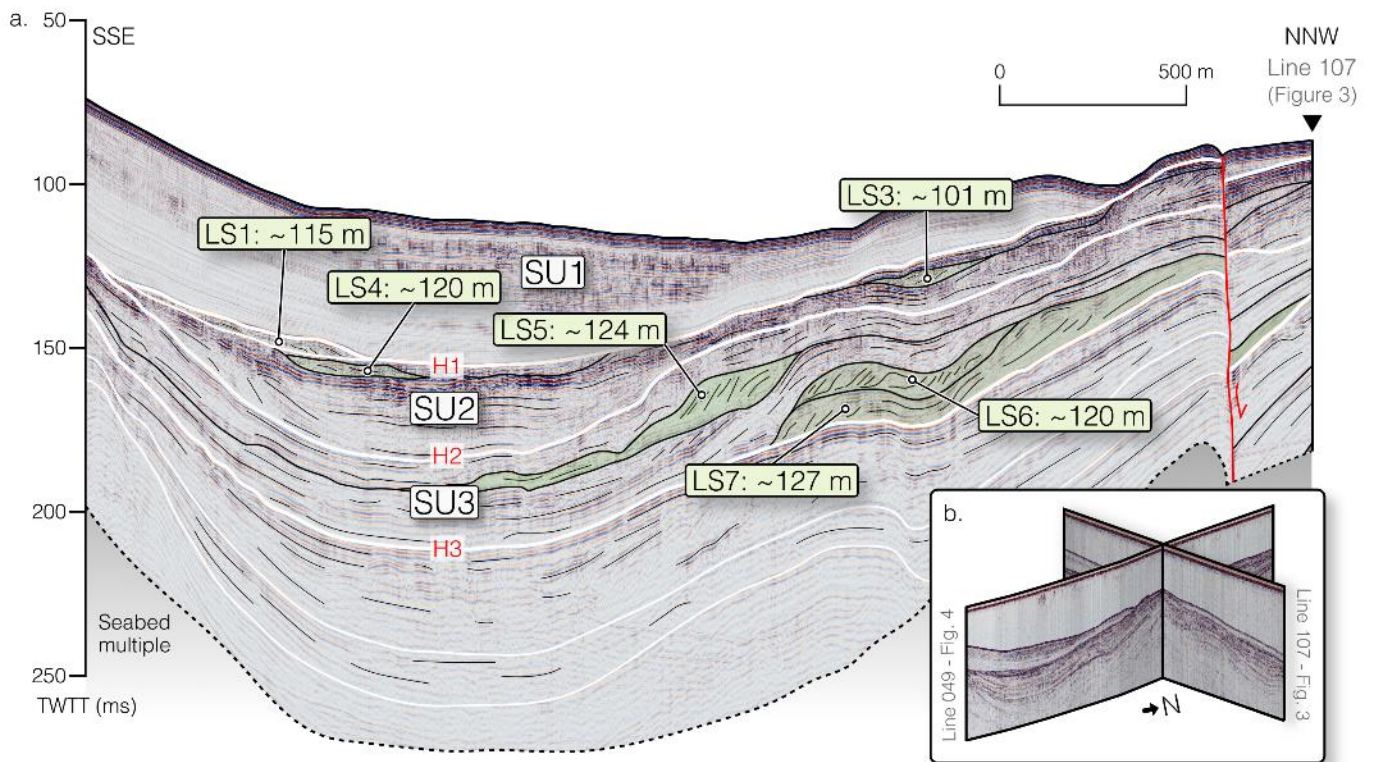
911 **Figure 2:** a) Regional tectonic map of the North Gulf of Evia, Central Greece. Major active
 912 normal fault zones highlighted in purple. Moment tensors of recent $M_w > 5$ earthquakes from
 913 the USGS database (<https://earthquake.usgs.gov/earthquakes/search/>). CFS = Coastal Fault
 914 System, AF = Atalanti Fault, APFZ = Aedipsos-Politika Fault Zone. Onshore fault traces
 915 compiled from a number of studies and databases (Galanakis et al., 2025; Ganas et al., 2013;
 916 Kranis, 2007) and primary field study. Offshore faults from Caroir et al., (2024). c) Bedrock
 917 geology of the Western Basin of the North Gulf of Evia (after IGME, 2006) and offshore

918 seismic reflection data profiles used in this study (see Supplementary Figure S5 for profile
 919 numbers). Fault slip vectors after Kranis (2007) and Arkitsa terrace outlines after
 920 Papanastassiou et al. (2014). KVF = Kamma Vourla Fault, AKF = Agios Konstantinos
 921 Fault, ArF = Arkitsa Fault.

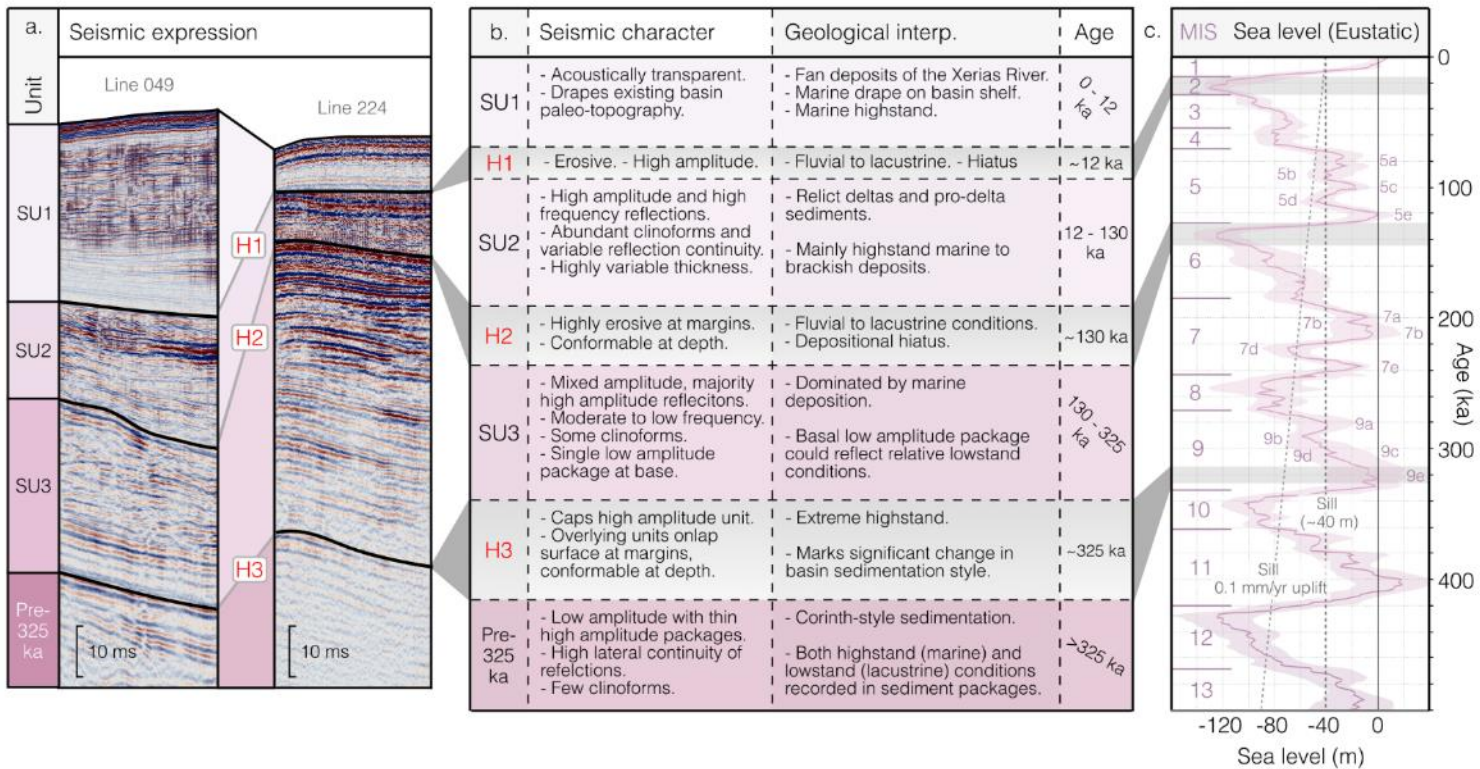


922 **Figure 3:** Schematic cartoons showing clinoform package geometries on a basin slope
 923 generated following a fall in relative sea level (RSL) from t_1 to t_2 to generate lowstand

924 packages (a) and a rise in RSL (b) to generate highstand packages. Modified based on
 925 Catuneanu (2002). c. Seismic interpretation of Line 107 (WATER II) showing 7 identified
 926 lowstand packages and 2 marked highstand intervals. Clinoform packages shaded based on
 927 highstand or lowstand attribution. Indicated depths are the rollover point of the clinoform
 928 package (i.e. base level indicator) based on seismic velocities of 1500 m/s and 1800 m/s for
 929 seawater and sediment respectively. Lowstand sequences are only considered for the age
 930 model in the footwall of the minor normal fault zone in the west of the seismic line. d.
 931 Detailed view of lowstand package interpretation with correlation to eustatic sea level curve
 932 of Spratt and Lisiecki (2016). See Supplementary Figure S6 for uninterpreted seismic section.



933 **Figure 4:** Seismic interpretation of Line 049 (WATER II) with the application of the
 934 sequence stratigraphic framework defined in the adjacent line (107) of Figure 3. Marked
 935 depths correspond to rollover point of clinoform package. b. 3D model showing the
 936 geometric interaction between Line 107 (Figure 2) and Line 049 shown in a. See
 937 Supplementary Figure S7 for uninterpreted seismic section.



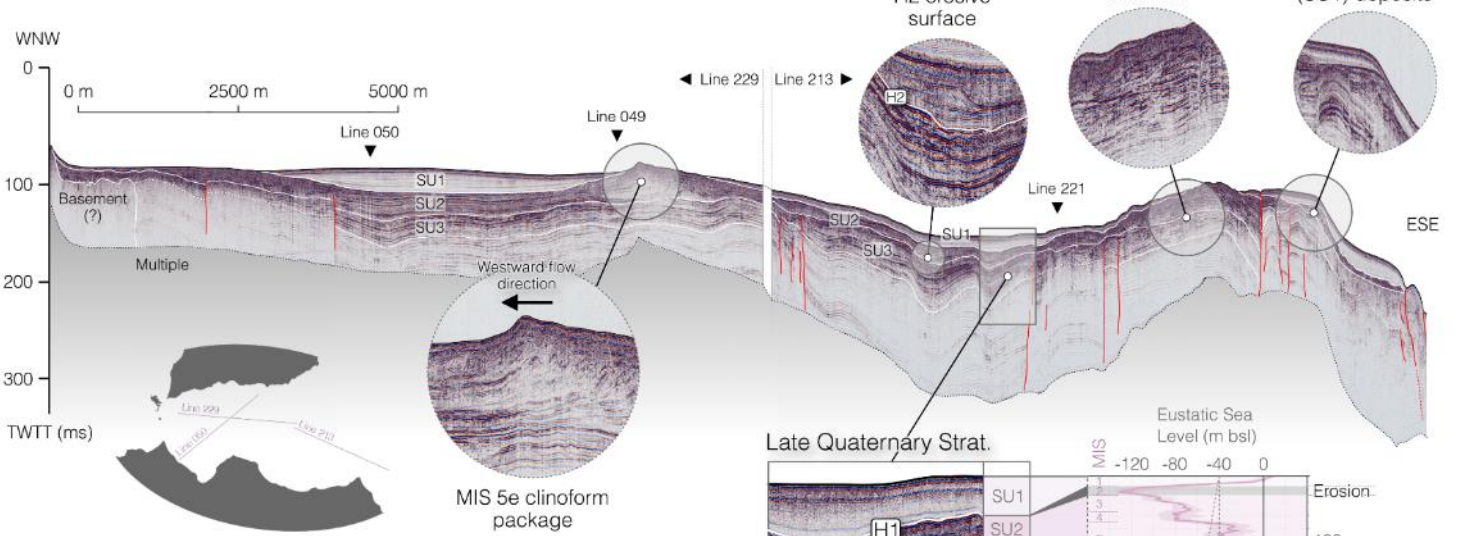
938 **Figure 5:** a. Seismic expression of upper syn-rift stratigraphy including seismic horizons
 939 (H1-3) and seismic units (SU1-3). b. Description of seismic character of each unit and
 940 horizon, geological interpretation of each unit and horizon and age attributed to each unit and
 941 horizon based on correlation to the eustatic sea level curve of Spratt and Lisiecki (2016)
 942 shown in c. Further seismic examples of mapped surfaces can be found in Supplementary
 943 Figure S2.

944

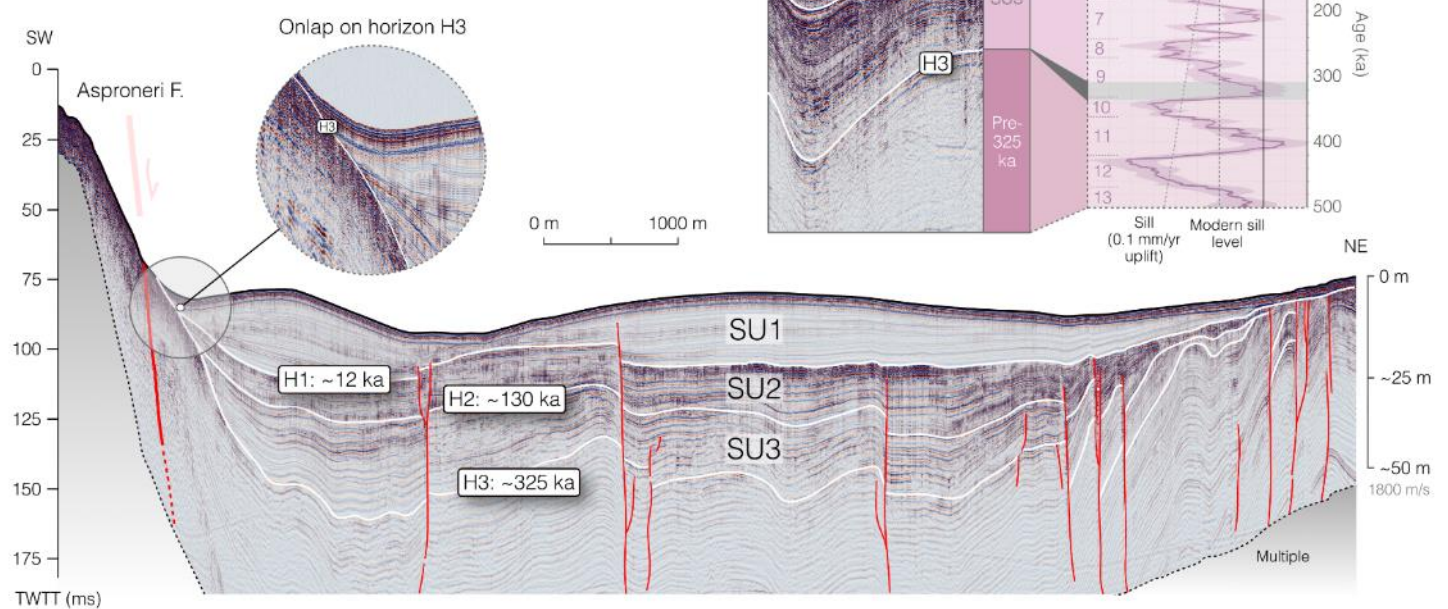
945

946

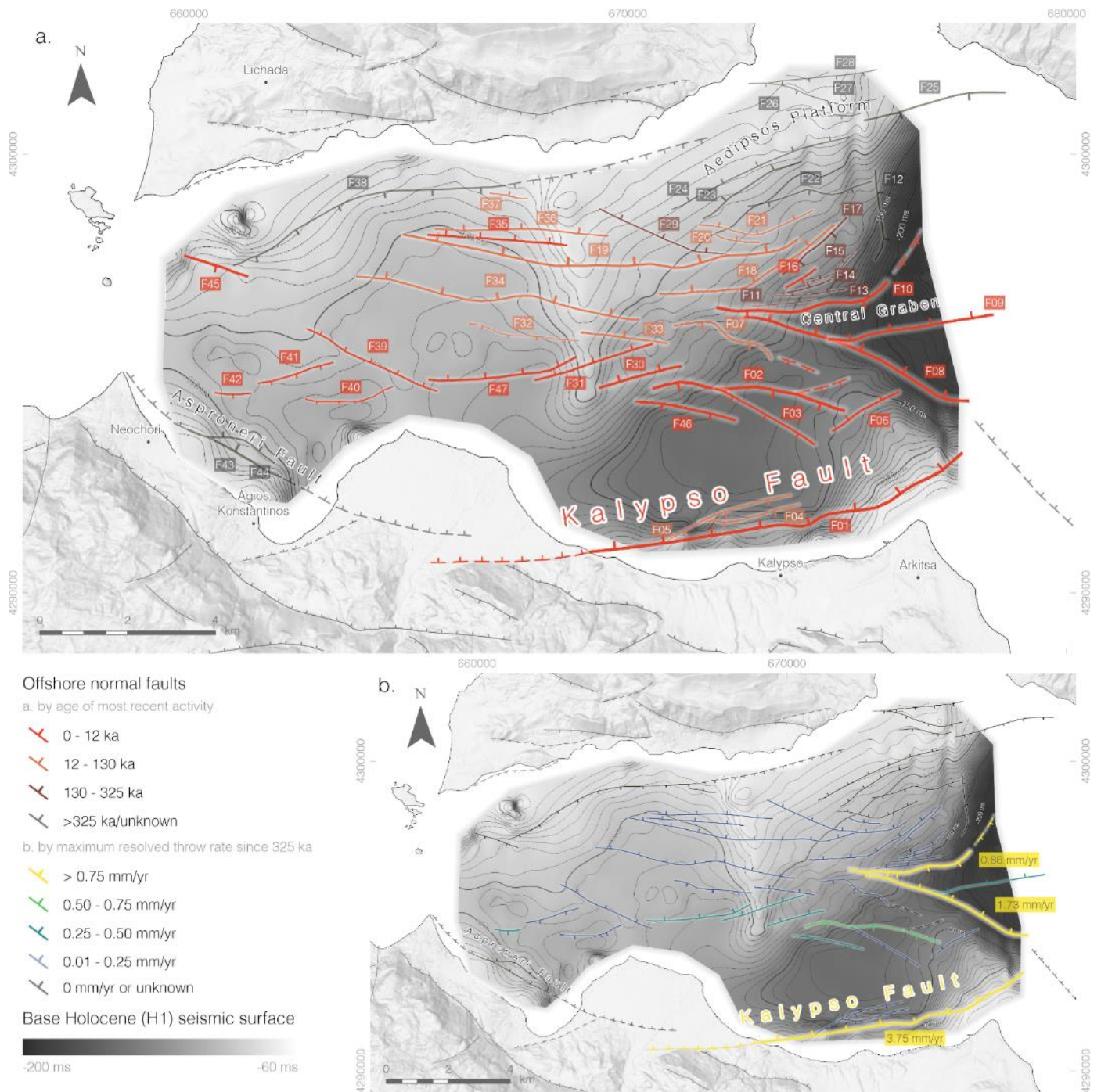
a. Axial seismic line: Line 213 & Line 229



b. Across basin seismic line: Line 050



947 **Figure 6:** a) Axial seismic reflection profile along the Western Basin (Lines 213 and 229)
 948 showing typical seismic sedimentary character, clinoform packages, variable Holocene
 949 deposit styles, and major depocenter locations. Stratigraphic age correlation (Figure 3) shown
 950 as inset with sea level from Spratt and Lisiecki (2016). b) Across-basin seismic reflection
 951 profile (Line 050) showing basin structure including Asproneri Fault and high fault density in
 952 NE. See Supplementary Figure S8 and S9 for uninterpreted seismic sections.

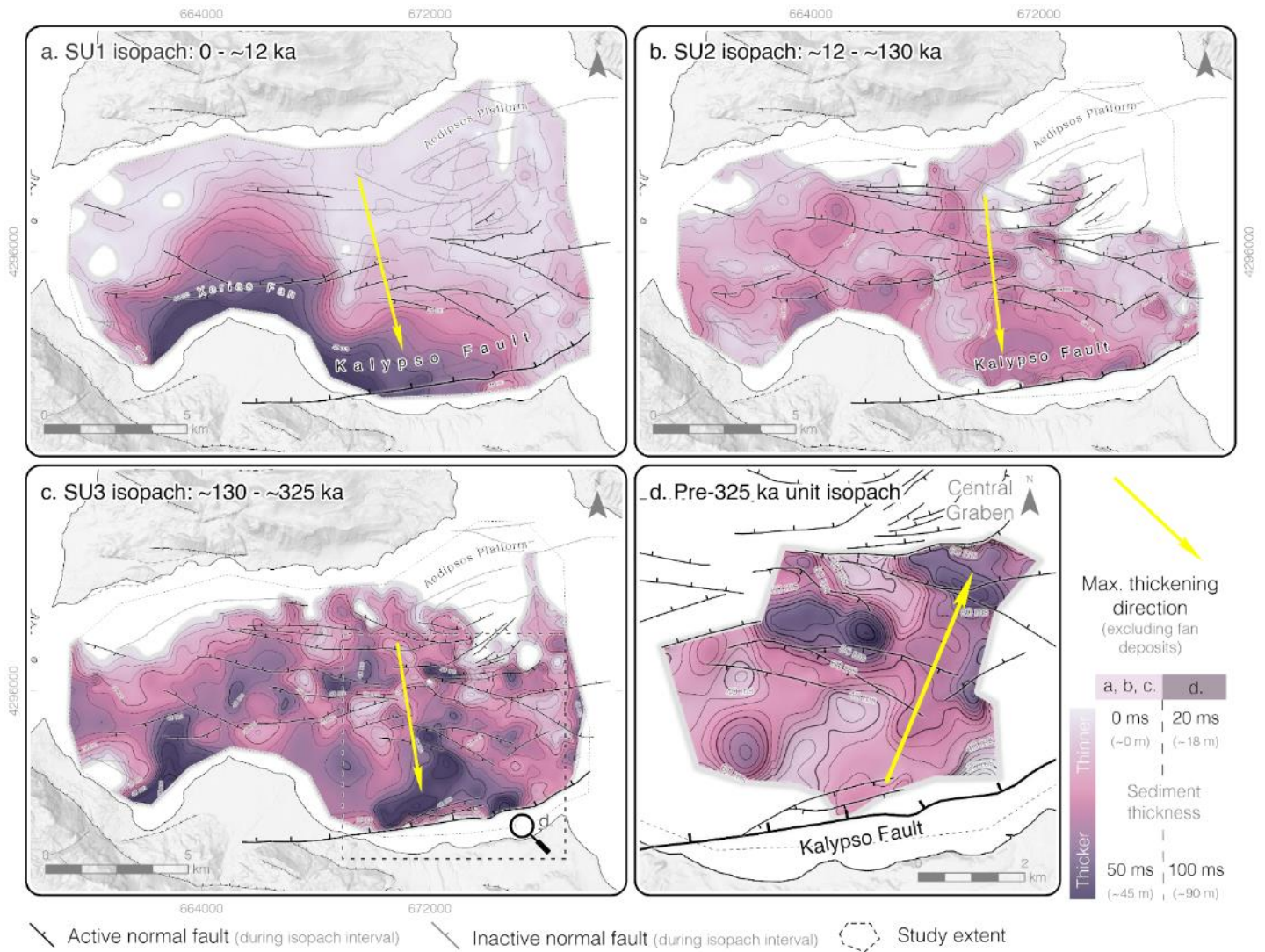


953

954 **Figure 7:** Map of offshore fault network identified in this study on depth to base Holocene
 955 (H1), effectively showing pre-Holocene basin geometry (without tectonic or compactional
 956 subsidence correction). a) Faults coloured by most recent activity based on offset of youngest
 957 key seismic horizon outlined in Figure 6. b) Faults coloured by maximum resolved throw rate
 958 over a given interval since ~325 ka (H3) based on throw rates calculated for each key seismic

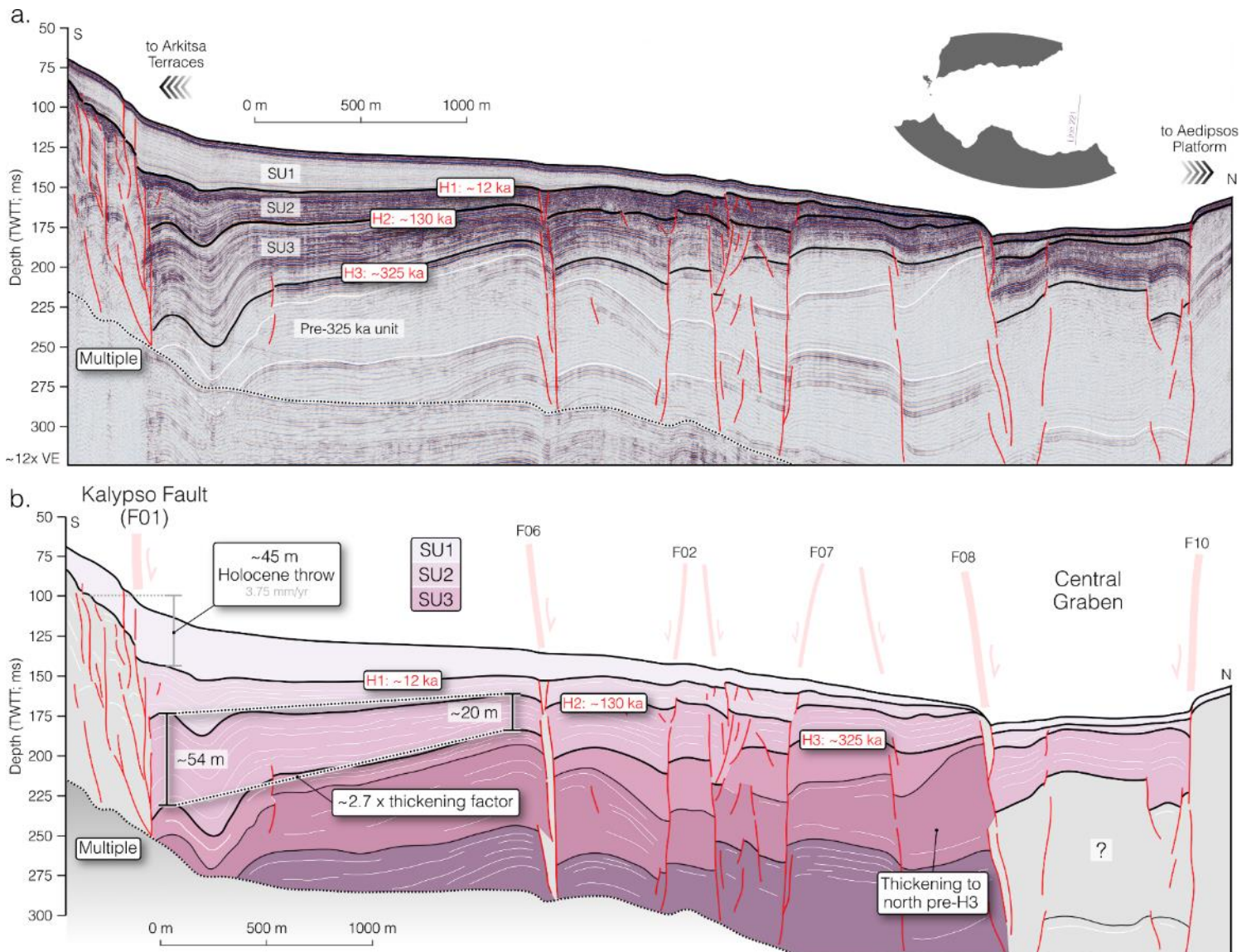
959 horizon (H1-3). See Supplementary Figure S3 for detail on the generation the H1 surface and
 960 Supplementary Table S1 and S2 for further detail on each mapped structure.

961

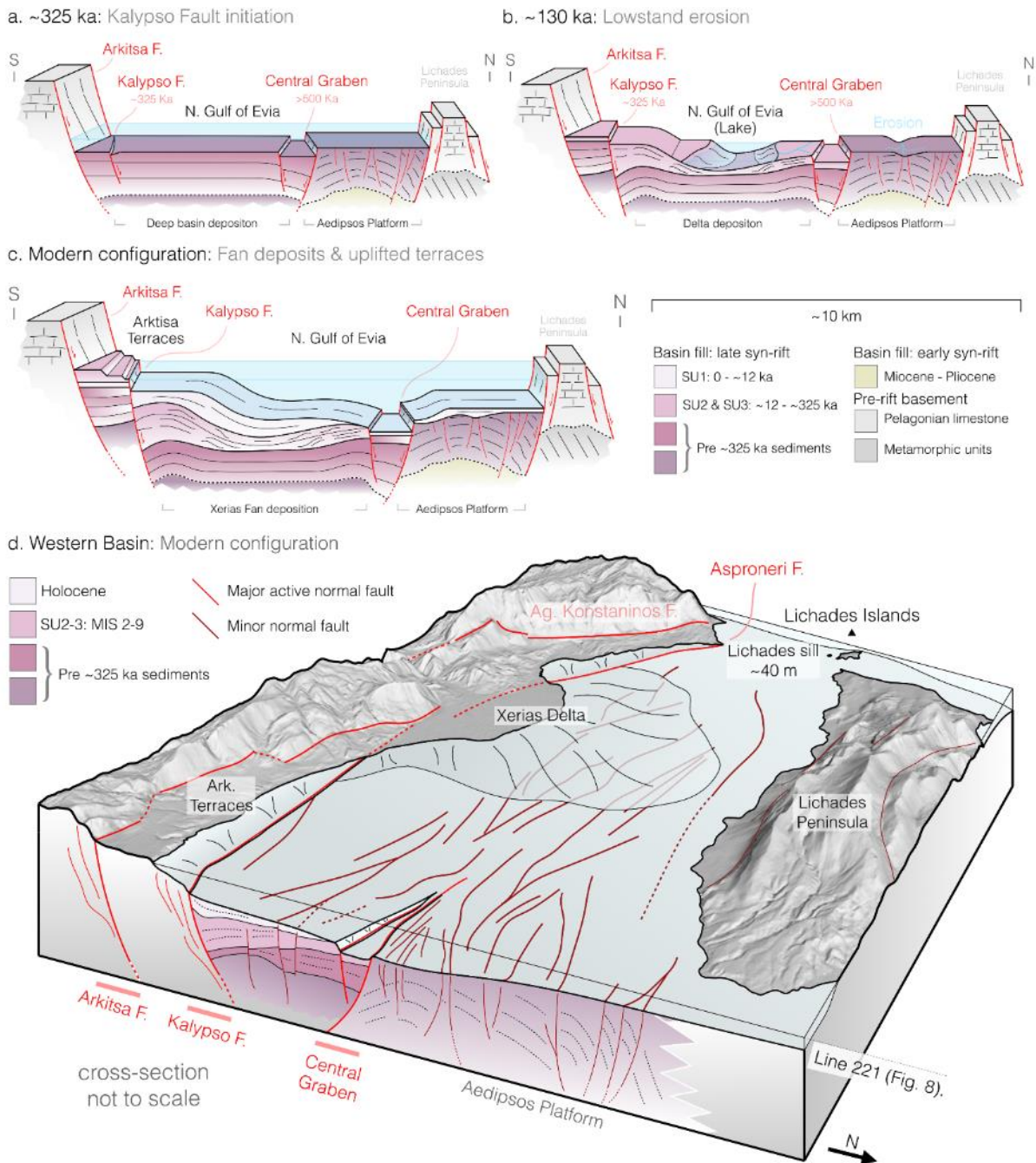


962 **Figure 8:** Isopach maps showing sediment thickness between the three major mapped
 963 surfaces in this study (a, b and c) and a package underlying the ~325 ka surface that is only
 964 apparent in the southeast of the study area (d). White area within study boundary indicates
 965 zero thickness.

966



967 **Figure 9:** a) Seismic reflection Line 221 with key surfaces (H1-3), seismic units (SU1-3) and
 968 faults shown. b) Interpreted section of line 221. The major Kalypso Fault Zone is shown in
 969 the south and active Central Graben in the north. SU1-3 thicken towards the Kalypso Fault
 970 (south), older packages with unassigned ages thicken towards the Central Graben (north). See
 971 Supplementary Figure S10 for uninterpreted seismic section.



972

973 **Figure 10:** a-c) Schematic evolutionary block models showing structural and sedimentary
 974 development of the Western Basin near Arkitsa at ~325 ka (MIS 9e; b), ~130 ka (late-MIS 6;
 975 c) and the modern configuration of the basin (d). a) Three-dimensional summary model of the
 976 modern Western Basin of the North Gulf of Evia showing fault network, key structures and
 977 modern topography. 2x vertical exaggeration. Cross-section not to scale. Looking towards
 978 240° at 25° pitch.